Multiscale Experiments: State of the Art and Remaining Challenges

R. Agrawal

H. D. Espinosa[1]
e-mail: espinosa@northwestern.edu

Department of Mechanical Engineering,
Northwestern University,
2145 Sheridan Road,
Evanston, IL 60208-3111

In this article we review recent advances in experimental techniques for the mechanical characterization of materials and structures at various length scales with an emphasis in the submicron- and nanoregime. Advantages and disadvantages of various approaches are discussed to highlight the need for carefully designed experiments and rigorous analysis of experimentally obtained data to yield unambiguous findings. By examining in depth a few case studies we demonstrate that the development of robust and innovative experimentation is crucial for the advancement of theoretical frameworks, assessment of model predictive capabilities, and discovery of new physical phenomena.
[DOI: 10.1115/1.3183782]

1 Introduction

In the past two decades, significant research efforts have been directed toward device and nanomaterial characterization following the generally acclaimed notion of "smaller is stronger." Experimental and computational studies revealed strong size-dependent material properties as the characteristic dimension of the structure approached 100 nm. These findings were particularly relevant in the context of miniaturization and design of novel micro- and nanosystems. Beyond their mechanical strength, nanostructures exhibit highly improved electrical, photonic, and thermal properties as compared with their bulk counterparts. Here we will focus on experimental approaches developed primarily to perform *mechanical* characterization at small size scales and their connection to computer simulations.

Two approaches have been pursued to explore the nanoscale world—experimental and computational; however, a gap remains between the two approaches, which preclude one-to-one comparisons. For instance, from computational studies, unique phenomena, such as pseudoelasticity, shape memory effects, and surface stress-induced phase transformation of nanowires have been reported in the literature [1–3]. These are attributed to factors such as larger surface to volume ratios, the prominence of surface stresses, etc. Unfortunately, experimental verification of many of these predictions is still not available. This gap between experimentation and simulations is rooted in several factors. First, it is extremely challenging to perform nanoscale experiments with desired resolutions and well-defined boundary conditions, particularly on specimens with characteristic size below 50 nm. By contrast, it is computationally very expensive to model atomistic systems as large as the ones experimentally investigated. Furthermore, the time scales (e.g., strain rates) at which nanoscale experiments and simulations are performed differ by orders of magnitudes. These limitations are being overcome gradually with simultaneous development of more sophisticated experimental techniques and improvement in parallel computing capabilities. Computationally, multiscale methods are also under development, bridging large variations in spatial domains. The differences in temporal domains are also addressed by implementing quasistatic conditions in experiments, as well as simulations. Second, simulations are mostly performed on idealized nanostructures, which might not be the case in real life. For example, most of the computational studies have been performed on pristine defect-free nanowires. They do not account for the inevitable random distribution of defects, arising from nanowire synthesis. Therefore, the experimentally observed mechanical response can greatly deviate from the computationally-predicted behavior. From an experimental perspective, such differences between simulations and experiments, at the nanoscale, can be reduced by (i) designing the experiments with well-defined loading and boundary conditions so that the complementary modeling effort can be pursued with minimal assumptions; (ii) testing specimens in a size regime, which can be modeled atomistically; (iii) having *in situ capability with desired spatial and temporal resolution so that the observed mechanical response can be directly correlated with the nanostructure—this also provides information about pre-existing defects and their evolution under loading to be incorporated in the computational models. Here, we will discuss the development and evolution of experimentation to characterize the mechanical behavior across various size scales.*

This article is outlined as follows. From the perspective of experimentation at the device scale, the characterization of radio-frequency micro-electromechanical system (MEMS) switches is briefly discussed. Then, experiments and simulations performed toward the understanding of plasticity size effects in thin films and single crystal micro-/nanopillars are presented. Section 2 focuses on one-dimensional nanostructures, covering two main aspects: the size effects observed in elastic/plastic behavior of nanowires, and the effect of atomic structure and its defects on the ultimate strength of carbon nanotubes. Finally, we conclude with some remarks on further developments needed to fill in the gap between experimentation and theory.

2 Experiments at the Device Scale

In the current era of miniaturization, focus has been directed toward the development of small scale micro-/nano-electromechanical systems (MEMS/NEMS) due to their smaller size, shorter time response, higher performance, and reduced energy requirements. These systems incorporate one-dimensional and two-dimensional nanostructures as their building blocks. For example, thin films, nanowires, nanotubes, etc. have been used and incorporated to conceptually demonstrate high performance transducers, logic circuits [4], optoelectronic [5], and piezoelectric [6] devices. Experimentation at different scales, starting from the device level down to the component level, is required to establish the reliable performance of any given device. For example, at the device level, MEMS-based radio-frequency (RF) switches have

[1]Corresponding author.

Contributed by the Materials Division of ASME for publication in the JOURNAL OF ENGINEERING MATERIALS AND TECHNOLOGY. Manuscript received February 24, 2009; final manuscript received June 10, 2009; published online September 1, 2009. Review conducted by Hussein Zbib.

been extensively studied. These switches are electrostatically actuated at frequencies as high as 100 kHz and, in some applications, operated at extreme temperatures ranging from room temperature to −40°C [7]. A capacitive RF-MEMS switch is in essence a micromachined capacitor with a moving top electrode, which can be mechanically modeled as a thin membrane clamped at the boundary. From an electromechanical perspective, this membrane behaves like a mass-spring system, actuated by an electrostatic force. Various techniques to characterize thin films have been developed, as will be discussed in Sec. 3; however, device level characterization is still crucial to be able to identify material properties and residual stresses resulting from the microfabrication process. For instance, the temperature during device packaging can reach 200°C [8], which leads to significant residual stresses that can affect the postpackage device performance. Extensive on-chip experimentation revealed that the life of these switches is limited by stiction between the metallic film and the dielectric substrate layer rather than the mechanical fracture or fatigue [9]. Low actuation voltages increase the lifetime of MEMS switches. However, the actuation voltage is related to the device geometry, mechanical properties, and residual stress state. Espinosa et al. [10] pursued a combined experimental-computational modeling approach to characterize the response of a membrane constituting the moving component in RF-MEMS switches. The membrane was first characterized by measuring its dimension and topography using optical full field profilometry. A novel device level membrane deflection experiment was then performed using a nanoindenter to deflect the film and to measure the load as a function of displacement. Load was measured with a resolution of a fraction of a micro-Newton and displacement with subnanometer resolution. By fitting the experimentally obtained load-deflection curves, membrane elastic properties and the state of residual stress were identified. In a second study, the authors pursued multiphysics modeling to reveal that an optimized out-of-plane profile of the membrane can be used to control stress relaxation and to yield minimal actuation voltage sensitivity to temperature changes, keeping the pull-in voltages within practical limits [7,10].

This example of RF-MEMS switches highlights how device level experiments can lead to a fundamental understanding of device performance and functionality. In the rest of this article, we focus on physical understanding gained at the component level, particularly in thin films, nanowires, and nanotubes, which are the building blocks for nanodevices.

3 Size Scale Plasticity in Metallic Thin Films and Single Crystal Pillars

Reducing the scale at which experimental testing is performed has been a developmental process over the past two decades. Earlier efforts focused on thin films to study the effect of film thickness on their elastic and plastic response to mechanical loading. Various novel phenomena were unveiled by the studies on thin films, which gave rise to the general notion that smaller is stronger. In this section, we discuss the understanding of plasticity size effects in *fcc metallic* thin films gained over the past few years. Figure 1 summarizes different experimental techniques employed in the study of thin films, their limitations, and their connection to theoretical models.

The effect of thickness on film strength was first reported in the late 1980s by Doerner et al. [11], who performed experiments on metallic aluminum and tungsten thin films. In the case of aluminum, the film strength was reported to increase with decreasing film thickness at both low and high temperatures. On the contrary, the strength decreased with decreasing thickness for the tungsten films. In this study, the metallic films were deposited on silicon substrates. Two different techniques, which emerged around the same time in the early 1980s, were used in these experiments for the sake of comparison. The first one, developed by McInerney and Flinn in 1982 [12] involved the measurement of substrate

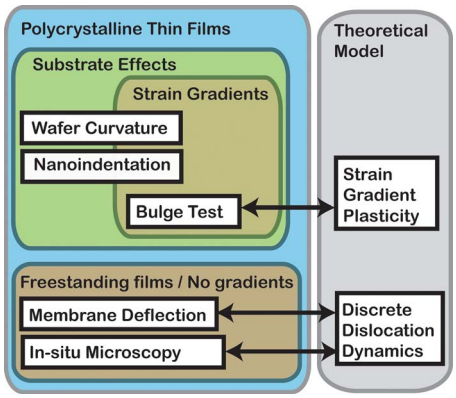

Fig. 1 A schematic summarizing the main experimental techniques developed for testing thin films and the corresponding theoretical models

curvature. In this method, a laser beam is scanned across the area of interest on the substrate, and the reflected beam is monitored by a position sensitive photodetector to deduce its curvature. To perform the mechanical test, thin film specimens were prepared by depositing the material of interest on a substrate with a different coefficient of thermal expansion. The stresses were then induced by heating, as different thermal expansion coefficients of the film and the substrate lead to deformation gradients at the interface. The second method was nanoindentation, which emerged with the development of the "nanoindenter" in 1983 [13]. This instrument continuously monitors the displacement of the indenter head as the load is applied. The load-displacement curve is then analyzed to calculate hardness, elastic modulus, and time-dependent deformation properties such as creep [13]. The results obtained for aluminum and tungsten thin films on silicon substrates revealed the dependence of mechanical behavior on film thickness, but with some uncertainties. First, it was not confirmed if the observed effect was due to the changing film thickness or due to the implicit change in grain size with the thickness. If the results were attributed to the changing grain size, then one would expect Hall–Petch type relationships for both the aluminum and the tungsten thin films, which was not the case. Second, wafer curvature measurements predicted higher strengths as compared with indentation measurements, indicating that the underlying substrate played an important role in strengthening the film. Third, it was realized that the nanoindentation technique yielded good results for soft materials, such as aluminum; however, the values reported for harder materials were too high [14]. It was thought that very high hydrostatic pressures at the point of contact just below the indenter could cause local densification or phase transformations leading to nonlinear effects, thereby, making it difficult to study the elastic/plastic properties [14]. Lastly, in both these experimental techniques, strain gradients were present due to nonuniform applied displacement fields.

Venkatraman and co-workers [15,16] separated the effects of film thickness and grain sizes on the strengthening of thin films. They applied the same wafer curvature technique on aluminum thin films deposited on silicon substrates and varied the film thicknesses while maintaining the same grain size [15]. They found that strengthening was inversely proportional to the film thickness. While these tests were still susceptible to the effect of the underlying substrate, the ambiguity of changes in grain size was removed.

In 1992, Oliver and Pharr [17] introduced an improved analytical method to correctly determine hardness and elastic modulus from nanoindentation load-deflection curves. The Oliver–Pharr method was initially developed for studying bulk materials; however, many researchers adapted it to investigate thin films. For example, Suresh et al. [18] studied copper thin films of different

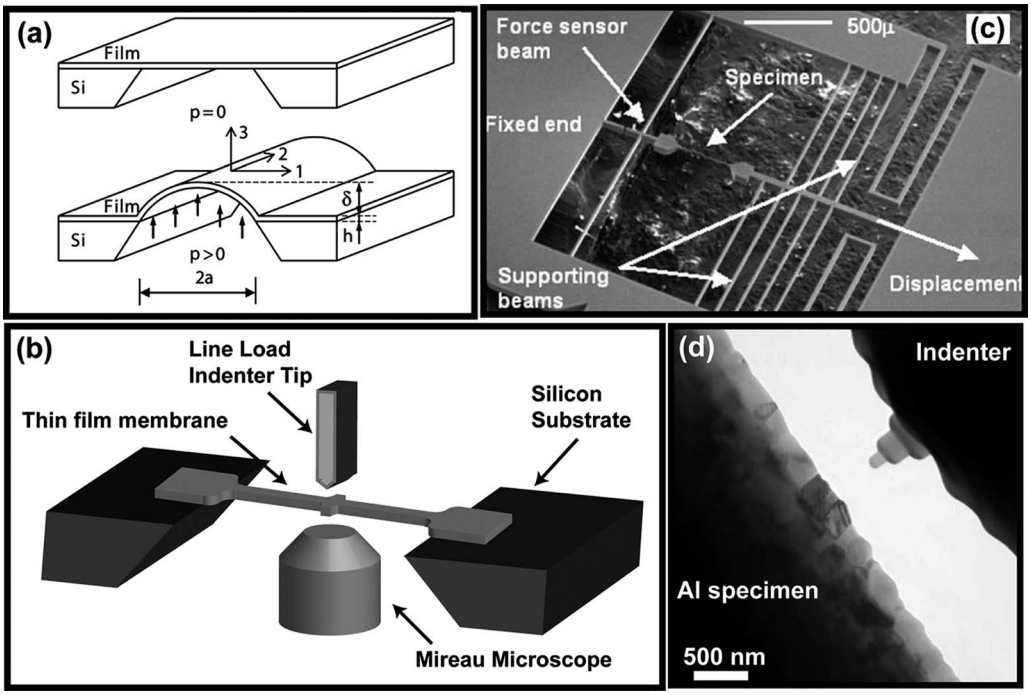

Fig. 2 Schematic showing plain strain bulge test before and after application of uniform pressure; (*b*) schematics of membrane deflection experiment; (*c*) a SEM micrograph of the MEMS-based testing setup; (*d*) a low magnification TEM image showing the *in situ nanoindentation* (Permissions: (*a*) reprinted with permission from Xiang and Vlassak [25] © 2006 Elsevier Ltd.; (*c*) reprinted with permission from Haque and Saif [31] © 2002 Acta Materialia Inc. published by Elsevier Science Ltd.; and (*d*) reprinted with permission from Minor et al. [32] © 2006 Nature Publishing Group)

thickness but with similar grain sizes on silicon substrates. They observed displacement bursts during the indentation process indicative of dislocation nucleation. The resistance to indentation was reported to increase with decreasing film thickness, consistent with the strengthening observed earlier by wafer curvature studies. Gouldstone et al. [19] reported similar results for thin films of polycrystalline aluminum and also performed postmortem analysis using transmission electron microscope (TEM) and atomic force microscope (AFM). Detailed TEM observation demonstrated that the indentation response of the thin films was composed of purely elastic behavior with intermittent microplasticity. The accuracy of these nanoindentation-based results was found to depend on several parameters, such as film and substrate properties, indentation depth as a function of total film thickness, and elastic mismatch between the film and the substrate [20,21]. In general, the nanoindentation-based studies qualitatively reinforced the notion that the strength of thin films increases with decreasing film thickness; however, the presence of the underlying substrate and strain-gradient effects still introduced uncertainties in the interpretation of results. Further details and results obtained through wafer curvature and nanoindentation studies can be found in an earlier review by Vinci and Vlassak [22], who was involved in the development of another technique called the "bulge test."

To remove the strengthening effect of the underlying substrate and associated strain gradients, Xiang et al. [23–25] employed the bulge test technique, which was developed [26,27] in the early 1990s to determine the Young's modulus and Poisson's ratio of thin films. In this method, freestanding thin films are prepared by micromachining processes [28]. The films are then deflected by applying a uniform pressure, which results in a plane stress loading scheme (Fig. 2(*a*)). By measuring the deflection of the center of the membrane as a function of applied pressure, the in-plane stress-strain response is deduced analytically. The effect of film thickness, surface passivation, and grain size on the plastic behavior of freestanding *coarse-grained* electroplated copper thin films was studied using the bulge tests. For the copper thin films, both the yield stress and the Young's modulus were found to increase with decreasing film thickness [23]. The yield stress of unpassivated films was found to vary with film thickness, which was attributed to implicit reduction in grain size in agreement with the Hall–Petch relationship [25]. On the contrary, the passivated films showed prominent size effect on loading and a discrete Bauschinger effect on unloading [25]. The passivation layers were found to stop dislocation annihilation from the surface by blocking slip bands at the film-passivation interface. It was hypothesized that the stresses associated with the blocked slip bands increased the resistance to forward plastic flow on loading and caused reverse plastic flow (Bauschinger effect) on unloading. Using the bulge test technique, Wei et al. [29] studied *nanocrystalline* copper thin films with a grain size of approximately 39 nm, as opposed to the coarse-grained electroplated copper thin films studied earlier [24]. Yield stresses of 410 ± 10 MPa were reported for the nanocrystalline thin films as opposed to a value of 300 MPa obtained for coarse-grained films. Also, the yield stresses were not found to depend on film thickness, which confirmed that the size dependence observed for coarse-grained films was due to the reduction in grain size associated with reduced thickness [29]. From a theoretical viewpoint, they applied the strain-gradient plasticity theory developed by Fleck and Hutchinson [30] and found that it could accurately capture the effect of film thickness, but failed to predict the Bauschinger effect observed in the unloading of passivated films.

Plasticity size effects in freestanding FCC films, in the absence of applied strain gradients, were investigated by Espinosa et al. [33–37] through a new technique called the "membrane deflection experiment" (MDE). With this technique, the complexity associated with strain-gradients and substrate effects were removed. Microfabrication techniques were used to prepare freestanding thin film specimens of different materials, widths, and thicknesses. The

films were designed so as to ensure uniaxial tensile stresses in the gauge section of the specimen (Fig. 2(*b*)). A nanoindenter was used to mechanically deform the freestanding thin films. To exclude the effect of grain size and grain boundary density, the average grain size was maintained constant and independent of film thickness. The tests were instrumented with a Mireau microscope such that film deformation, localization, and fracture were observed in real time and correlated with the mechanical response. Using the MDE, the stress-strain behavior of polycrystalline films of copper, aluminum, and gold, in the range of 0.2–1.0 μm, were examined. The yield stress was found to increase with decreasing film thickness, and a strengthening size scale of one over film thickness was identified. These results were in general agreement with other studies for fcc thin films on substrates [18,38]; however, in the case of gold, a major transition in material inelastic response was revealed as the film thickness was reduced from 1 μm to 0.3 μm. Yield stresses as high as 220 MPa were measured for 0.3 μm-thick film, as opposed to 90 MPa for 1 μm-thick film exhibiting deformation localization and strain softening [37]. Postmortem scanning electron microscope (SEM) and TEM studies revealed deformation bands in membranes with thickness of 1 μm. By contrast, the 0.3 μm and thinner films did not exhibit deformation bands, but underwent plastic deformation via grain boundary nucleated dislocations [39].

These findings were also consistent with the *in situ* electron microscope studies conducted by Haque and Saif [40,41] using a microfabricated loading frame. Their setup consisted of a freestanding thin film sample cofabricated with a microtensile stage (Fig. 2(*c*)). The thin film specimen was bonded to a force sensor beam at one end and to a set of supporting beams at the other end; all the beams were made of single crystal Si. Displacements were imposed on one end of the stage and were then transmitted to the force sensing beam through the specimen. The deflection of the force sensing beam was monitored to deduce the load in the specimen. They performed tensile tests on freestanding gold and aluminum thin films with film thicknesses ranging from 50 nm to 480 nm and grain sizes ranging from 15 nm to 75 nm. For films with grain sizes smaller than 50 nm, they reported nonlinear elasticity with lower elastic modulus, lack of work hardening, and brittle failure. In the 200 nm-thick aluminum films, TEM observations revealed significant dislocation activities within grains of size 150 nm and higher. No such activity was observed for 100 nm and thinner films with grain sizes of 50 nm or smaller, demonstrating that the deformation in thinner films with smaller grain sizes was governed by grain boundary-based mechanisms rather than dislocation motion. For aluminum thin films in the thickness range of 30–50 nm, they also reported a monotonic decrease in elastic modulus, nonlinear elastic behavior, and decreasing ductility with grain size [31]. Upon unloading, the films followed the loading stress-strain path with small plastic deformation. Upon reloading, there was negligible strain hardening. To account for the observations, they proposed a model in which the grain boundary region is elastically softer than the grain interior, and it becomes increasingly softer with increasing tensile strain. This model was based on two assumptions: (i) the grain boundary to grain interior ratio is large so that grain boundary compliance dominates; and (ii) the grain size is small so that the stress for dislocation nucleation follows the Hall–Petch model. This model is, therefore, complementary to the dislocation-based mechanism proposed by Espinosa et al. [39] for large grain sizes ($\sim$200 nm). Espinosa et al. [39] performed three-dimensional discrete dislocation dynamics (DDD) simulations of grains representative of the system microstructure and associated characteristic dimensions to qualitatively describe the experimentally observed effects. The DDD simulations revealed two key aspects explaining the origin of plasticity size effects: (i) the onset of plasticity is governed by dislocation nucleation controlled process; and (ii) the hardening rate is controlled by dislocation source exhaustion resulting from the size and boundary effects. It is important to point out that a direct comparison with the DDD simulations was possible for this set of experiments, as the strain gradients were absent.

In addition to the grain boundary sliding and dislocation nucleation/annihilation effects, a novel mechanism of "stress-assisted discontinuous grain growth" was reported by Gianola et al. [42,43], who studied the deformation behavior of nanocrystalline aluminum freestanding thin films under tension. Their experiments employed a customized tensile testing setup, which offers precise grip alignment with five degrees of freedom to ensure that a tensile state of stress is induced in the specimen [44]. A screw driven picomotor, with resolution of less than 40 nm, was used to apply a controlled displacement to one end of the thin film. A load cell with μN resolution was used to measure the applied loads. For the same film thickness and average grain size, they observed reduced strength and increased ductility in *some* of the specimens. Postmortem TEM studies revealed that the extended plasticity was the outcome of discontinuous grain growth leading to a microcrystalline structure in the presence of stresses. Another recent study *in situ* TEM [45], using the microfabricated loading frame developed by Haque and Saif [40,41], reported up to 100% recovery of plastic deformation in gold and aluminum thin films after unloading. The process of recovery was found to be time-dependent and thermally activated. A proposed mechanism for the significant plastic recovery was based on heterogeneous grain boundary diffusion due to the presence of impurities and inherent variations in the grain structures. It was asserted that inhomogeneous grain boundary diffusion can lead to severe internal stresses during loading that can serve as driving force for plastic strain recovery upon load removal. This *in situ* setup with the microfabricated loading frame was a good attempt to relate the mechanical behavior to the microstructure of the thin films; however, it suffered from one major design limitation. In order to measure applied load, the electron beam needed to be displaced from the specimen to the clamped-clamped single crystal Si beam, whose deflection was used to identify the force. Therefore, it was not possible to perform high resolution TEM imaging while simultaneously loading (and measuring the load-displacement response) the specimen.

In the aforementioned studies, uncertainties arising from the presence of strain gradients and substrate effects were ruled out one after another to gain an in-depth and clear understanding of plasticity at the nanoscale. However, ambiguities due to variation in grain size and their random orientation remained. Postmortem TEM analysis assisted in building hypotheses attributing to dislocation-based or grain boundary-based mechanisms. What was still missing was the *in situ* capability, which can provide a direct correlation between the mechanical response and microstructural evolution. The relevance of performing *in situ* characterization was established in the mid-1980s by Robertson et al. [46] when they observed atomic level phenomenon, such as microtwin formation at stress concentrations, dynamic transfer of slip across a grain boundary [47], and formation of vacancy type dislocation loops [48]. Matsukawa and co-workers [49–51] investigated the interactions of stacking fault tetrahedrons with moving dislocations using *in situ* methods. These *in situ* studies focused on observation of phenomena associated with plasticity, but more technological development was needed to simultaneously measure the load-displacement response.

In an attempt to correlate the mechanical response of thin films with their microstructural evolution, in 2001, Stach et al. [52] developed a nanoindenter for performing mechanical tests *in situ* an electron microscope. Using this setup, Minor et al. [53,54] observed the discrete microstructural events and correlated them with the load-displacement characteristics. Figure 2(*d*) shows a TEM image demonstrating the experimental setup. They observed staircase instability, i.e., a sudden increase in the displacement for the same applied load, and asserted that the instability corresponds to the onset of plasticity and dislocation nucleation in a grain that is defect-free prior to loading. Further insight into the onset of

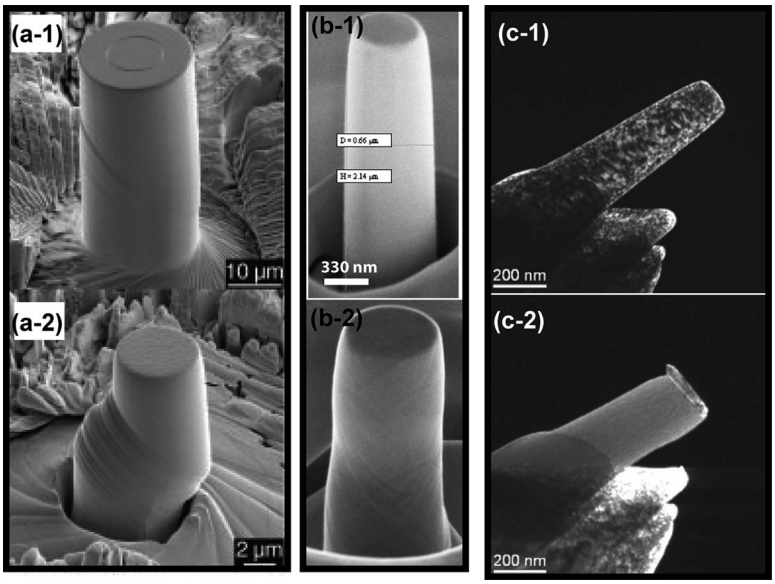

Fig. 3 (*a*1) A SEM image of a 20 μm diameter Ni pillar showing slip events at ~4% strain an engineering stress of ~50 MPa; (*a*2) SEM image of a 5 μm diameter Ni pillar after testing at ~19% strain where a rapid burst of deformation occurred in less that 0.2 s. Engineering stress as high as 130 MPa was observed; (*b*1,2) SEM image of a 660 nm Au pillar before and after deformation. In these experiments, yield stress as high as 500 MPa was observed for a 400 nm pillar; and (*c*1,2) TEM images acquired during *in situ* TEM nanoindentation tests on a 160 nm diameter Ni nanopillars. Before the test (*c*1), the nanopillar had high dislocation density, which disappeared after first loading. Stresses as high as 1.0 GPa were reported. (Permissions: (*a*) reprinted with permission from Uchic et al. [56] © 2004 American Association for the Advancement of Science; (*b*) Reprinted with permission from Greer et al. [57] © 2005 Acta Materialia Inc. published by Elsevier Ltd.; and (*c*) reprinted with permission from Shan et al. [58] © 2008 Nature Publishing Group).

plasticity was gained later [32] via experiments on dislocation free volume of polycrystalline aluminum. These experiments revealed that the theoretical shear strength is reached before dislocation nucleation. The authors also observed that submicrometer grains of aluminum with high dislocation density are also capable of sustaining shear stresses as high as the theoretical strength. This finding was in contradiction to the general notion that a defect-free volume is necessary to achieve theoretical strength.

To decouple the effect of grain boundary-based mechanisms from size related effects, single crystal studies were conducted by Uchic et al. [55,56] on nickel (Ni) micropillars using a nanoindenter with a flat head punch. Ni pillars ranging from 0.5 μm to 40 μm in diameter were prepared by focused ion beam (FIB) milling of bulk material (Fig. 3(*a*)). The pillars were compressed in a displacement-controlled fashion using the nanoindenter until plastic deformation was achieved in the finite deformation regime. Postmortem SEM observations revealed that the fundamental process of plastic deformation is significantly modified for micropillars with diameters smaller than a few tens of micrometers. It was hypothesized that the plastic deformation behavior is controlled by the escape of dislocations through the surface of the micropillars. Size effects on FCC *single crystals* were revealed by these micropillar compression tests, which provided a leap in understanding of dislocation-mediated plasticity in single crystals. Following this work, Greer et al. [57] refined the methodology to further reduce pillar diameter to sizes as small as 250 nm (Fig. 3(*b*)). Figure 4(*a*) shows the experimentally obtained stress-strain plots for pillars with decreasing diameters. The authors reported flow stress as high as 4.5 GPa, which is a significant fraction of the theoretical strength of gold. Strengthening of the pillars was explained based on a "dislocation starvation" hypothesis. This hypothesis asserted that the annihilation of dislocations through the surface leads to a state in which higher stresses are then required to nucleate new dislocations and further deform the crystal plastically.

The experimental technique employed in these studies was ex situ; hence, postmortem TEM studies were further performed to observe the structure of the slip bands in the nanopillars. Unfortunately, uncertainties associated with the effect of TEM sample preparation and the possible instability of dislocation networks prevented unambiguous verification of the starvation hypothesis. By employing discrete dislocation dynamics simulation, Espinosa and co-workers [59,60] provided a plausible explanation for the plasticity size effects and the typical staircase stress-strain behavior observed experimentally (Fig. 4(*a*)) in gold micropillars. The initial conditions, geometry, loading, and the boundary conditions employed in the simulations allowed for a direct comparison with the experimental results, Fig. 4(*b*). The model was composed of a pre-existing random network of jogged dislocations, which were relaxed before application of the load. The computationally obtain dislocation network was equivalent to what in the literature is referred to as Frank networks and constituted the first attempt to eliminate the artificial introduction of Frank–Read sources of random strength. In the simulations, load was controlled with step increases of 50 MPa. Figure 4(*b*) shows the computationally obtained stress-strain response for three cases with the same initial dislocation density but different initial network configurations. Strain bursts separated by regions of nearly elastic loading are evident and consistent with the experimental findings. From the simulations, the evolution of the dislocation network revealed sequential shutdown of the sources as dislocations escaped through the surface and explained the physical phenomena behind the dis-

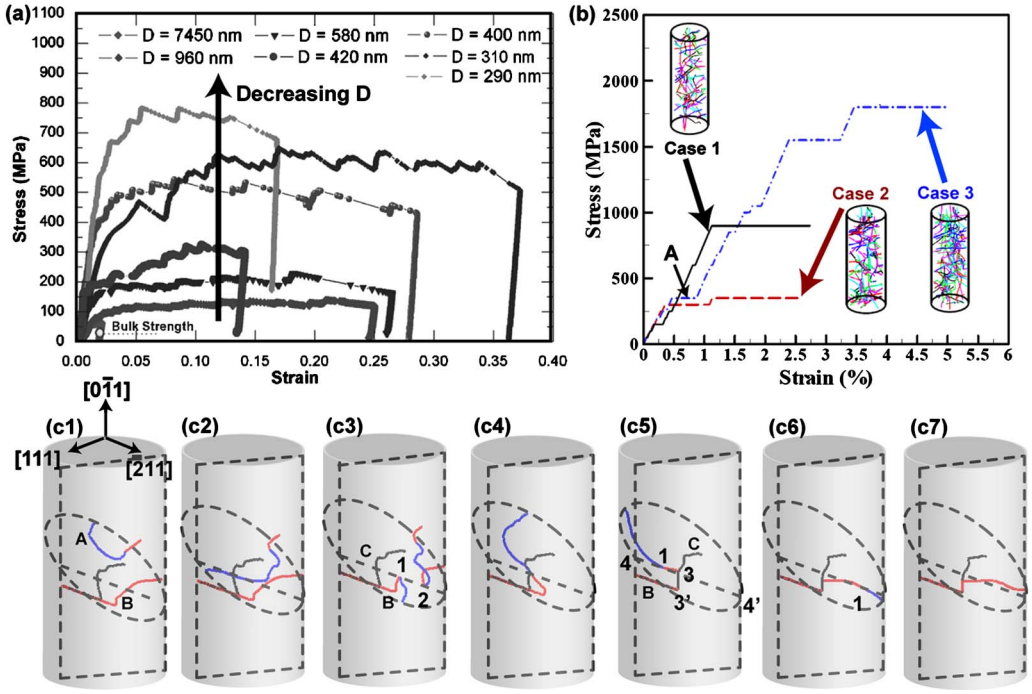

Fig. 4 (*a*) **Experimentally obtained stress-strain behavior of gold pillars under compression, showing the increasing yield stress with decreasing diameter;** (*b*) **Computationally obtained stress-strain plots for 400 nm pillars with same dislocation density, but different initial dislocation configurations;** (*c*) **a series of images showing the dislocation evolution associated with strain bursts (see text for detailed explanation) (Permissions:** (*a*) **reprinted with permission from Greer and Nix [62], http://link.aps.org/doi/10.1103/PhysRevB.73.245410.** © **2006 The American Physical Society;** (*b*) **reprinted with permission from Tang et al. [60], http://link.aps.org/doi/10.1103/PhysRevLett.100.185503.** © **2008 The American Physical Society).**

location starvation hypothesis. The evolution process corresponding to the strain burst, marked by A in Fig. 4(*b*), is shown by a series of images in Fig. 4(*c*). In these figures, only a few dislocations involved in the step formation are shown. Dotted ellipse corresponds to (111) type slip plane, and the dotted rectangle denotes a second slip plane aligned with the loading axis. At a compressive stress of 350 MPa, Fig. 4(c1) and 4(c2) (colored online) shows that one dislocation line (A, blue) started gliding and approached another dislocation line (B, red). The collinear interaction [61] of these two dislocation lines generated two spiral sources 1 and 2 (Fig. 4(c3)). Source 1 was constrained by the junction formed by B (red) and C (black) dislocation lines; however, source 2 was free to move and annihilated as it reached the surface of the pillar (Fig. 4(c4)). The constrained motion of source 1 caused another collision between two dislocation lines (B, red and C, black) resulting in another junction 33′ (Fig. 4(c5)). This active source 1 moved on the glide plane along the intersection line 44′, resulting in plastic deformation at constant load (Fig. 4(c5) and 4(c6)). The source finally shuts down via annihilation at the surface after a period of loading (Fig. 4(c7)). After that annihilation, purely elastic straining occurred until another dislocation source was created or activated, leading to the staircase type stress-strain response. Additional details on the mechanisms leading to this phenomenon are reported in Ref. [60].

This mechanistic interpretation was experimentally validated by means of the *in situ* nanoindentation setup developed by Stach et al. [58]. These authors performed compression tests on single crystals of Ni and observed the above phenomenon, which they called "mechanical annealing" (Fig. 3(*c*)). They found that a crystal with high dislocation density can be made defect-free, i.e., mechanically annealed, in the initial phase of loading. They hypothesized that mechanical loading activates pre-existing dislocations, which move and annihilate at the surface of the specimen. This was a remarkable observation revealing the annihilation of dislocations though the surface of nanopillars, in agreement with the dislocation starvation mechanism observed in earlier experiments and confirmed by DDD simulations.

4 Experimental Techniques for Studying One-Dimensional Nanostructures

As summarized in Sec. 3, customized instrumentation and novel approaches were employed to characterize two-dimensional thin films. To pursue single crystal studies, one-dimensional nanopillars (up to 250 nm in diameter) were tested using nanoindentation-based method. As opposed to pillars, thinner nanowires and nanotubes with larger aspect ratios cannot be tested via nanoindentation due to the likelihood of buckling or bending. Therefore, further reduction in characteristic size poses new challenges for experimental studies. Various direct and indirect techniques have been developed and a variety of one-dimensional nanostructures have been studied. These experimental techniques will be discussed next in context of two particular materials—zinc oxide (ZnO) nanowires and carbon nanotubes (CNTs). The same techniques have also been used to study nanostructures made of other materials. A brief summary of other materials studied is provided in Sec. 4.3.

4.1 Size Dependent Elastic Properties of Zinc Oxide Nanowires. Zinc oxide nanostructures exhibit remarkable semiconducting, piezoelectric, and biocompatible properties, which have drawn the attention of many scientists and engineers. Research efforts envision the implementation of ZnO nanostructures as building blocks of high performance optoelectronic devices [5], logic circuits [4], piezoelectric devices [6], nanoresonators, and electromechanically coupled nanocantilever sensors [63]. For re-

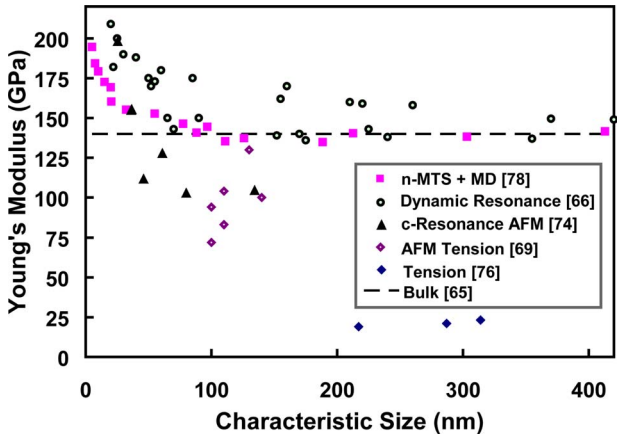

Fig. 5 Summary of Young's modulus of ZnO nanostructures as a function of characteristic size obtained by different experimental techniques

liable design of such devices, a thorough knowledge of the mechanical response of these nanostructures is desirable. ZnO is chosen in this article to illustrate various nanoscale experimental techniques and the successful one-to-one comparison with atomistic simulations. Various techniques involving dynamic resonance *in situ* TEM, atomic force microscopy, nanoindentation, and MEMS-based testing have been used to characterize the elastic response of ZnO nanostructures. Each technique involves different assumptions for interpretation of the experimentally acquired data. As a result, discrepancies in the experimentally measured values for Young's moduli are large—values ranging from 20 GPa to 250 GPa have been reported with no consensus for a given characteristic size. Figure 5 shows the scatter in Young's modulus values reported by different experimental techniques. Some studies report size-dependent behavior, while some do not. Each of these techniques, their findings, and limitations will be discussed next.

Bai et al. [64] performed experiments on [0001] oriented ZnO nanobelts and reported a size-independent bending modulus of 52 GPa, which is far lower than the expected bulk value of 140 GPa [65]. They used *in situ* dynamic resonance tests, developed in late 1990s, in which the nanostructure under study is singly clamped and actuated either thermally or electrostatically (Fig. 6(*a*)). The nanobelts were attached to a gold electrode and were manipulated to be placed opposite to another gold electrode. An alternating voltage with tunable frequency was applied across the two electrodes. Since the induced charges on the tip of the nanobelts oscillated at the frequency of the applied voltage, mechanical resonance was induced when the applied frequency matched the natural vibration frequency of the nanobelts. As the integration time needed for capturing the TEM image is much larger than the vibration cycle, blurring is observed in the TEM images, and the envelope (i.e., the amplitude) of the vibrations is used to infer the Young's modulus. Using the same experimental method, Chen et al. [66] later reported that the elastic modulus of [0001] oriented ZnO nanowires depends on the nanowire diameter. They found that the Young's modulus increased from 140 GPa to 220 GPa as the nanowire diameter decreased from 550 nm to 17 nm. To explain the size dependence, they proposed a core-shell model for the nanowires, with a stiffer shell as compared with the core. From fitting their experimental data to this model, they predicted a shell thickness of 4.4 nm with a modulus of 1.5 times the bulk modulus. The limitation of this model lies in the size range studied experimentally. Due to fitting to limited experimental data, the shell thickness turned out to be the radius of the smallest nanowire (NW) they tested, and the shell modulus was the modulus of this smallest nanowire [66]. This resonance based technique avoids the need of manipulating the specimens and provides direct visualization of the experiment. However, due to bending, the deformation is mainly gradient dominated, which has a more pronounced surface elasticity effect as compared with uniform axial deformation [66].

Atomic force microscopy based tests were also developed as AFM offers unprecedented force and displacement resolutions. Three main experimental configurations have been utilized to load nanostructures using an AFM cantilever: (i) the ends of the specimen are fixed to a substrate and load is applied in the plane of the substrate using the AFM in lateral force mode (Fig. 6(*b*)); (ii) the specimen is suspended on a microfabricated trench or a nanoporous membrane with both ends fixed and load is applied normal to the plane of the substrate using the AFM in contact force mode (Fig. 6(*c*)); (iii) nanotubes or nanowires are grown vertically directly from the substrate to create singly clamped cantilevers and the free end is displaced by the AFM probe in lateral force mode. In all the cases, the loading mode for the specimen is bending—three-point bending for the first two cases and simple bending for the third case. Ni and Li [67] reported a Young's modulus of 38.2 ± 1.8 GPa for ZnO nanobelts by three-point bending AFM tests, independent of the characteristic size. Song et al. [68] reported a slightly smaller value of 29 ± 8 GPa by bending singly clamped vertical ZnO nanowires using AFM. Hoffman et al. [69] used a modified approach to pull on the vertical nanowires by attaching them to an AFM probe using carbonaceous deposition inside the SEM chamber. They reported a Young's moduli of 97 ± 18 GPa for nanowires 100–140 nm in diameter. As one can notice, the Young's moduli obtained from AFM bending/tension tests are much smaller than the bulk value of 140 GPa. This is in direct contrast with the size dependence seen in the dynamic resonance tests performed by Chen et al. [66]. Recently, Zhou et al. [70] performed finite element simulations to show that there are different factors, which can contribute to the underestimation of Young's modulus by three-point bending tests. Some of these include the boundary conditions at the fixed ends of the nanowire, the aspect ratio of the nanowire, and the deflection of the nanowire at the point of loading.

Nanoindentation-based techniques also seem to be obvious natural choice for nanoscale testing. However, to characterize nanowires with small diameters and large aspect ratios, uniaxial compression is not suitable, as there is a significant likelihood of buckling. Instead, Stan et al. [74,75] used an indirect AFM-based method called "contact resonance AFM" in which a nanowire lying on a substrate is indented with an AFM cantilever in both axial and radial directions. In this method, a calibrated AFM probe is brought in contact with the nanowire, and a given load is applied. At this load, the driving signal for the AFM cantilever is generated using a lock-in amplifier to perform repetitive nanoindentation of the nanowire. The photodiode signal is also acquired by the lock-in amplifier, which is analyzed to measure the shift in resonance frequencies. This shift in frequency is then quantified in terms of contact stiffness between the AFM probe and the sample. The indentation modulus of the specimen is calculated from the contact stiffness, assuming a circular contact area between the AFM tip and the specimen. Using similar methodology in lateral AFM mode, they performed friction type measurements and reported the tangential shear modulus as well. For ZnO nanowires [74], they reported an increase in the radial indentation moduli, as well as lateral shear moduli for nanowires of diameters smaller than 80 nm. Their trends were similar to the results obtained earlier from dynamic resonance tests; however, the values reported for moduli were smaller. In particular, this methodology predicted a modulus of ~ 100 GPa corresponding to bulk, which is $\sim 70\%$ of the expected value of 140 GPa. This difference is attributed to the difficulty associated with precise measurement of the contact area between the AFM tip and the nanowire surface, as this contact area significantly affects the adhesion/capillary forces at the nanoscale and, therefore, the interpretation of results.

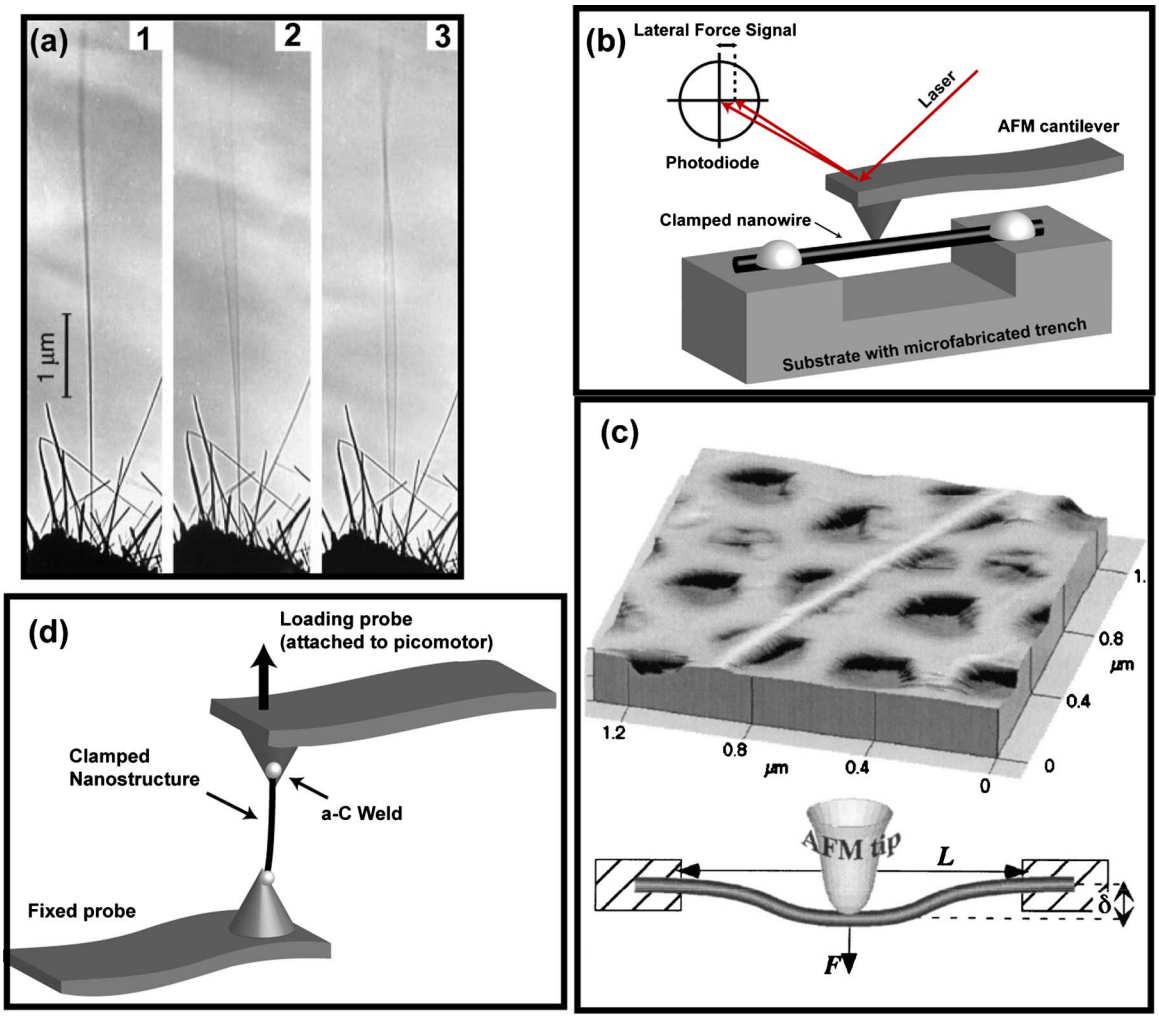

Fig. 6 (*a*) **SEM micrographs demonstrating the *in situ* thermal vibration tests. 1—freestanding nanotubes fixed at one end; 2—first mode of resonance; 3—second mode of resonance; (*b*) schematic representation of AFM-based three-point bending tests in lateral force mode; (c) schematic representation of AFM-based three-point bending tests in contact mode. Top figure shows the AFM image of a SWNT rope suspended over a polished alumina ultrafiltration membrane; (*d*) schematic representation showing the setup for *in situ* tension tests on an individual MWNT using two calibrated AFM probes. (Permissions: (*a*) reprinted with permission from Poncharal et al. [71]. © 1999 American Association for the Advancement of Science; (*c*) reprinted with permission from Salvetat et al. [72], http://link.aps.org/doi/10.1103/PhysRevLett.82.944. © 1999 American Physical Society).**

Desai and Haque [76] microfabricated a customized test-bed with two jaws between which the nanowire specimen was placed. One jaw was fixed and the other was attached to the middle of the device to which the displacement was applied [77]. A customized SEM stage was employed to apply displacements using a piezo-actuator. The force was deduced by observing the deflection of the device folded beams *in situ* an SEM. In their setup, the nanowires were first dispersed on a freestanding silicon dioxide (SiO_2) grid. A nanowire suspended across a hole in the grid was located and fixed on to the grid by FIB induced platinum deposition. The grid along with the nanowire was then manipulated and placed on the device. Instead of the nanowire being attached to the device, the grid was attached by platinum deposition. They reported a very small Young's modulus of ~20 GPa for nanowires of diameter 200–300 nm. This represents the lowest modulus reported in the literature for ZnO nanowires.

As the above paragraphs and Fig. 5 illustrate, the literature reports a variety of experimental techniques and findings that reveal discrepancies in the observed phenomena. The sources of error appear to be in (a) instrument calibration to measure applied loads and displacements; (b) fixing and mounting of samples; (c) measurement of nanowire diameter or cross-sectional area; and (d) applied boundary and loading conditions. The discrepancy in the size-dependent elastic behavior of ZnO nanostructures described above was resolved by Agrawal et al. [78] using a combined experimental and theoretical approach. They found that the Young's modulus increases from 140 GPa (bulk value) to 195 GPa as the nanowire diameter decreases from 80 nm to 5 nm [78]. At the core of resolving these discrepancies was the development of an experimental technique based on MEMS technology; the so-called nanoscale-material testing system (n-MTS) developed by Espinosa and co-workers [79–82]. The n-MTS is the world first to provide *electronic* measurement of load and deformation while allowing simultaneous acquisition of high resolution images of the atomic structure of specimens within the TEM (see Fig. 7(*a*)). The device facilitates uniaxial tensile loading under displacement control by means of thermal actuation. Load is measured, based on differential capacitive sensing, with a resolution of about 10 nN. The specimens are mounted on the device using a three-axis piezoelectric nanomanipulator, and the ends of the specimens are fixed by electron beam induced deposition (EBID) of platinum (Fig. 7(*b*)) [81]. As the load and displacements are measured elec-

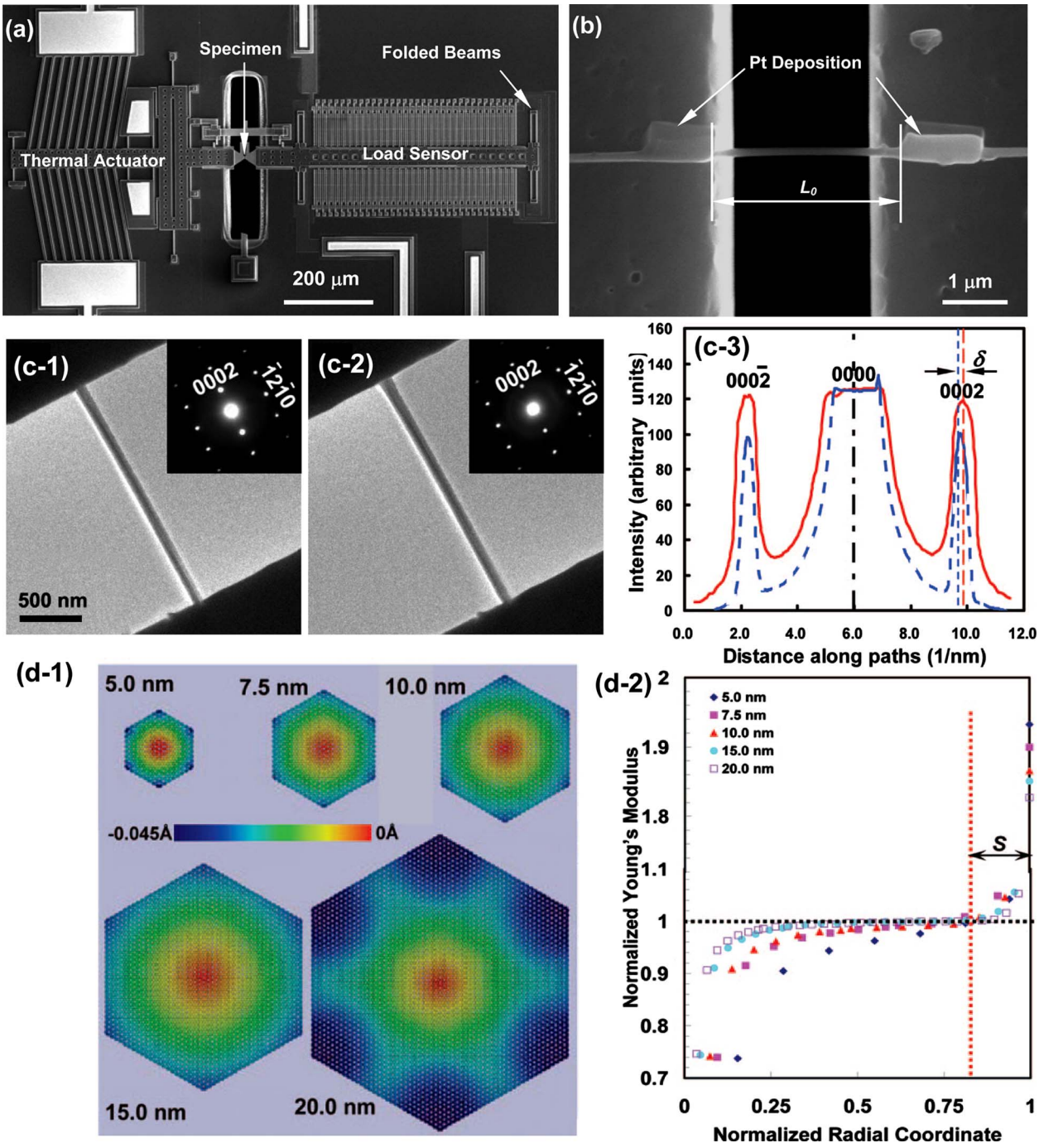

Fig. 7 (*a*) **SEM micrograph of MEMS-based nanoscale-material testing system to perform *in situ* TEM tests; (*b*) SEM image of a ZnO nanowire mounted on the n-MTS with e-beam induced deposition of platinum to fix the two ends; (*c*1,2) TEM images of the ZnO NW taken during a tensile test at 0% and ~2.5% strain. Inset shows the corresponding diffraction patterns; (*c*3) Intensity analysis of the diffraction patters shown in (*c*1) and (*c*2) along [0001] direction to measure the change in lattice constant; (*d*1) Contours of radial displacements, for nanowires of different diameters, after energy minimization; (*d*2) Young's modulus normalized with bulk modulus, as a function of normalized radial coordinate in each atomic layer. The shell thickness, *s*, is indicated. (Reprinted with permission from Agrawal et al. [78]. © 2008 American Chemical Society).**

tronically, high resolution TEM imaging of the specimen is possible, in real time, without the need for shifting the electron beam. Figure 7(*c*) shows the TEM images and corresponding selected area diffraction (SAD) patterns taken during the tensile loading experiment of a ZnO nanowire. Intensity analysis of the SAD patterns along the axis of loading was done to measure the changes in lattice constant and therefore calculate strain from an atomic perspective. The important features of this experimental method include (i) displacement-controlled loading; (ii) simple uniaxial state of stress which is straightforward to interpret; and (iii) simultaneous high resolution imaging to directly correlate the stress-strain response with the atomic structure of the specimen being tested. Due to these well-defined experimental conditions, a direct comparison with molecular dynamic (MD) simulations was made possible. Tensile tests were conducted on the [0001] oriented ZnO NWs with diameters ranging from 20 nm to 480 nm.

MD simulations were performed on nanowires ranging from 5nm to 20nm in diameter, with the 20 nm size bridging the gap between the experimentally tested and computationally modeled sizes. The experimental and computational findings are discussed next.

The experiments revealed a size-dependent elastic response with Young's moduli increasing from 141 GPa to 160 GPa, as the nanowire diameter decreased from 88 nm to 20 nm. For larger wires, the value was 139 ± 3.5 GPa, consistent with the bulk value of 140 GPa [65]. Complementing the experimental results, MD simulations predicted an increase in the Young's moduli from 169 GPa to 195 GPa, as nanowire diameter decreased from 20 nm to 5 nm. The atomistic analysis revealed that the nanowire surface reconstructs from bulk atomic positions, resulting in axial expansion and radial contraction of the nanowire under equilibrium. The extent of relaxation depends on the nanowire diameter. Due to this surface effect, the radial contraction on the nanowire surface is highly localized, leading to shortening of bond lengths, which makes the surface atoms elastically stiffer as compared with the inner core atoms. Figure 7(*d*) shows the radial displacements in the cross section of nanowires of different diameter at equilibrium and the corresponding effect on the Young's moduli of each wire as a function of its radial coordinate. These results were in general agreement with the core-shell model proposed by Chen et al. [66], but did not reveal a shell of fixed thickness. Instead, the size of the shell scaled with the wire diameter (denoted by *s* in Fig. 7(*d*)).

The combined experimental and MD results are shown in Fig. 5, along with other experimental data. From an experimental standpoint, the key to establish this connection included two main aspects: (i) the proper characterization of cross-sectional area of the nanowires, which was measured by SEM imaging of the fractured surface of the nanowire after the tensile test; and (ii) accurate measurements of strain at the atomic level by calculating the change in interatomic spacing from the diffraction patterns acquired during loading. The second aspect is attributed to the capability to simultaneously perform high resolution imaging while testing the specimen. In this study, the authors also found that carbon deposition [69] to weld the ends of the nanowires leads to hysteresis on repeated loading and unloading. This indicates that carbon welding is not strong enough to achieve fixed-fixed boundary conditions, and highlights some of the challenges in establishing standardized testing protocols for nanoscale testing.

As evident from the prior paragraphs, proper experimentation along with appropriate modeling, could resolve the inconsistencies reported in the literature and highlight the probable sources of error in experimentation at the nanoscale. This particular experimental approach using the n-MTS, exhibiting unprecedented force and displacement resolutions and simultaneous *in situ* electron imaging represents the current state of the art for characterization of one-dimensional nanostructures. More attributes of this kind of approach will be highlighted as we look into the mechanisms of carbon nanotubes next.

4.2 Ultimate Theoretical Strength of Carbon Nanotubes. The discovery of carbon nanotubes by Ijima [83] in the early 1990s gave rise to an entirely new paradigm for making devices at the nanoscale. The outstanding mechanical properties of CNTs are being exploited in a variety of applications ranging from high performance fibers [84] to nanoelectronics [85–88]. First principle calculations [89–92] predict that defect-free single-walled CNTs possess Young's modulus of ~ 1 TPa, tensile strengths greater than 100 GPa, and high fracture strains of 15–30% depending on the tube chirality. Unfortunately, early experimental work failed to demonstrate such outstanding properties as a result of limitations similar to those discussed for the case of nanowires. The inconsistencies between theory and experiments preoccupied the community for many years and directed modeling efforts to the analysis of defective atomic structures. As it will be shown in this section, true properties of CNTs were not revealed until more sophisticated experimental approaches were developed [93,94]. The techniques used for mechanical characterization of CNTs are similar to those already discussed in the context of ZnO nanowires.

For instance, *in situ* dynamic resonance tests with thermal actuation was used by Treacy et al. [95] to investigate the Young's modulus of multiwalled carbon nanotubes (MWNTs). The amplitudes of intrinsic thermal vibrations were measured as a function of the applied temperature. They tested arc discharged MWNTs and found Young's moduli ranging from 0.4 TPa to 3.7 TPa, with an average value of 1.8 TPa. Following this work, Poncharal et al. [71] also studied the Young's modulus of similar arc discharged MWNTs; however, they induced mechanical resonance by actuating the nanotubes via an ac electrostatic field within a TEM. The resonance frequencies were measured to deduce Young's moduli ranging from 0.1 TPa to 1 TPa. To overcome large deformation gradients associated with dynamic bending and to be able to capture the fracture behavior of nanotubes, AFM-based techniques have been applied.

Using the AFM-based bending technique previously described, Wong et al. [96] measured the Young's modulus, strength, and fracture strength of MWNTs lying on a substrate. They reported a Young's modulus of 1.28 ± 0.59 TPa and a fracture strength of 14.8 ± 8.0 GPa, which is well below the theoretically predicted value of 100 GPa. Walters et al. [97] suspended the nanotubes over a trench to overcome adhesion and friction between the specimen and the substrate. The Young's moduli measured ranged from 0.067 TPa to 1.31 TPa. Similarly, Salvetat et al. [72,98] deflected arc-discharge MWNTs vertically by dispersing them on a nanoporous alumina membrane with 200 nm pores and reported an average modulus of 0.81 TPa. An overlap exists among the Young's moduli values measured in different studies, and values as high as those predicted by theoretical studies have been achieved; however, fracture strain reported by these studies was still less than 20% of theoretical estimates. It was thought that AFM probes are likely to cause stress concentrations and to induce defects at the point of contact, thereby decreasing the overall strength.

To avoid strain gradients associated with bending and stress concentrations imposed by the AFM probes on the point of contact, Yu et al. [73] performed tensile tests on MWNTs *in situ* a scanning electron microscope. They used two AFM probes—a relatively soft one as a load sensor and a stiffer one as an actuator—attached to a piezo-based linear motor (as shown schematically in Fig. 6(*d*)). The two ends of the CNT were attached to the two probes and the test was performed in the SEM to measure the deflection of the soft AFM cantilever and the nanotube. From the stiffness calibration of the AFM probes, the force-deflection response was deduced. They reported a Young's moduli of 0.27–0.95 TPa, failure strength of 11–63 GPa, and failure strains between 2% and 13%. The low values of modulus were attributed to the defects introduced by oxidative pitting during nanotube purification. Theoretical calculations [99,100] have suggested that such defects can dramatically lower the modulus and decrease the failure strains. Recently, Ding et al. [101] used the same experimental technique to test *unpurified* arc-discharge grown MWNTs. They obtained an average modulus value of 0.95 TPa for the 14 tubes studied, which is in good agreement with the theoretical results; however, measured mean fracture strengths and failure strains were still only 24 GPa and 2.6%, respectively.

A modified version of the technique employed by Yu et al. [73] was used to study the tensile failure of *chemical vapor deposition* (CVD)-grown MWNTs [102,103]. Instead of attaching the nanotubes to AFM probes on both the sides, one end of the nanotubes was clamped by embedding it in epoxy glue. The free end was attached to the AFM probe and pulled upon until failure was observed. In this work, multishell failure was identified mostly involving the failure of all the shells, at low failure strains. The values reported for fracture strength of CVD-grown tubes were as

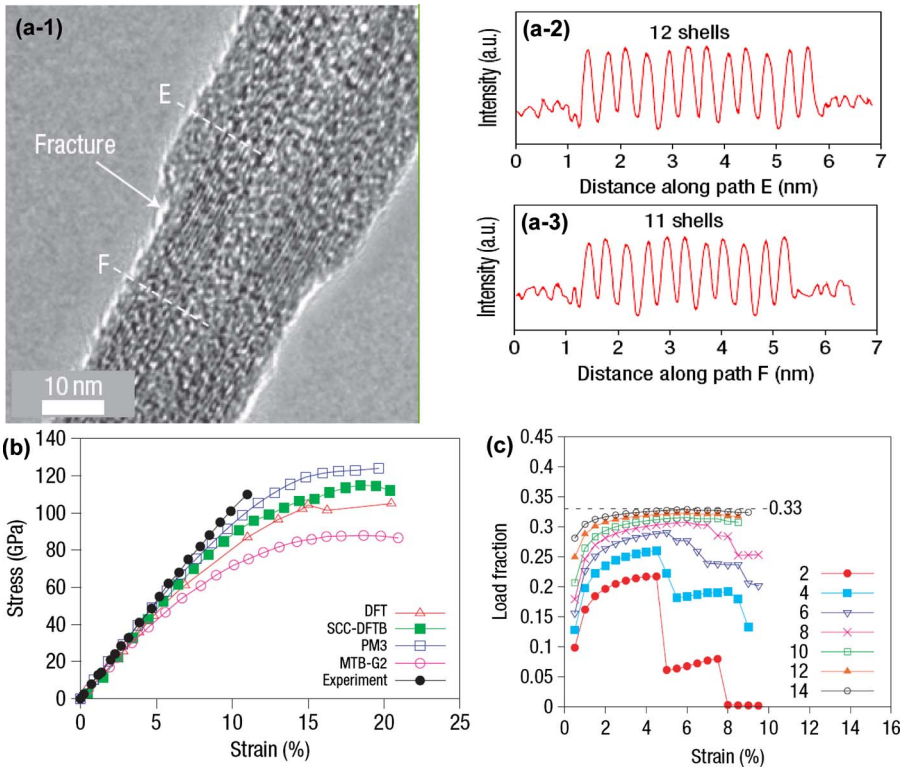

Fig. 8 (*a*1) TEM image of a MWNT after fracture; (*a*2,3) intensity profiles taken along the paths E and F in (*a*1) to count the number of shells before and after failure. (*b*) Stress-strain response comparing the experimental data with theoretical predictions; (*c*) computational calculation of load transferred to the inner shell of a double-walled nanotubes as a function of the number of cross-links. (Reprinted with permission from Peng et al. [93]. © 2008 Nature Publishing Group).

high as ~260 GPa, which is well in excess of the theoretical quantum-mechanical prediction of ~100 GPa. In this study, the number of load bearing shells was not characterized, and single-shell failure was assumed in the calculations. Under this assumption, high fracture strength appears to be the result of significant load sharing among the shells facilitated by the wavy shell wall resulting from the CVD synthesis method. However, if the cross-section of all the fractured shells is used to calculate fracture strength, the values are again well below the theoretical predictions.

These studies highlight the importance of knowing the characteristic atomic structure being tested and its failure mechanism for correct interpretation of the experimental data. This necessitates the development of high resolution *in situ* techniques so that the observed mechanical behavior can be directly related to the atomic structure under study. The n-MTS (Fig. 7(*a*)), developed by Espinosa and co-workers, provides this capability by performing TEM imaging with atomic resolution for proper characterization of the nanotube's chirality, the number of broken shells, and the failure mechanism. With this unique device, the computationally-predicted properties of CNTs were measured experimentally for the first time [93]. As shown in Fig. 8(*a*), high resolution TEM imaging and displacement-controlled loading made it possible to capture the failure of a single shell of a MWNT. Since only the outer shell of the nanotube was fixed at the welded ends, the nanotube failed via a telescopic or "sword-in-sheath" mechanism, where the outer shell broke leaving the inner ones intact. One key to be able to achieve theoretical strength was to ensure that the energy of the electron beam, used for imaging in the TEM, was kept below a threshold energy required to generate defects [104]. Also, the uniaxial tensile mode of loading allowed for high desired strains without inducing any bending artifacts. The number of failing shells was characterized by analyzing the intensity profiles along the cross section of the nanotubes (Fig. 8(*a*)). Observation of the single-shell failure was a remarkable achievement as this experimental result opened avenues for direct comparison with theoretical studies done on SWNTs. In these experiments, fracture strength of ~100 GPa and fracture strains of ~12% were measured, which are comparable to the theoretical calculations of nanotubes with small defects such as single vacancies or Stone–Wales defects. To make a close comparison, experimental data for a nanotubes with chirality very similar to computationally modeled [10,0] type single-walled nanotubes was chosen. Figure 8(*b*) compares the experimental stress-strain curve to the theoretical predictions made by different first principle approximations, such as density functional theory (DFT), the semi-empirical quantum-mechanical model PM3, the empirical second-generation modified Tersoff–Brenner (MTB-G2) potential, and self-consistent charge density functional-based (SCC-DFTB) tight binding. The agreement between the experimental curve and different quantum-mechanical models is very good, particularly with the PM3 model. The most noticeable difference is in the failure strain which can be attributed to presence of defects in experimentally tested nanotubes. For example, PM3 calculations show that even a single missing atom can reduce the fracture stresses from 124 GPa to 101 GPa and fracture strains from ~20% to ~13% [99]. Defects, on the contrary, introduced in a controlled manner can also lead to improved performance of the nanotubes. This was revealed by the same *in situ* TEM tests, as discussed in the next paragraph.

As it was found that electron beam irradiations, during *in situ* TEM experiments, can induce defects in the nanotubes, the study was extended to characterize the effect of electron irradiation on

nanotubes. The nanotubes were exposed to an electron beam of known current density at a set magnification for a given amount of time and the irradiation dose was calculated based on those parameters. By increasing electron dosage dramatic increases in load carrying capacity was identified. The phenomenon was attributed to irradiation induced cross-linking of multiple shells [93]. The cross-links help transfer the load from the outermost shell to the inner shells, resulting in a more uniform load sharing among different shells. The load sharing increased the overall stiffness of the nanostructure. These results were also verified by means of computational studies. The computational model predicted the load distribution between two different shells of a double-walled nanotube as a function of the number of cross-links. Figure 8(*c*) shows the effect of the increasing number of cross-link on the fraction of the load shared by the inner shell of a double-walled nanotube.

Complementing the aforementioned *in situ* studies, where single-shell failure was observed, Lee et al. [105] investigated monolayer graphene sheets, which in essence are unrolled single-walled carob nanotubes. The authors used AFM-based nanoindentation to probe the mechanical response of graphene sheets. Graphite flakes were mechanically deposited on a silicon substrate with a circular array of wells, patterned by reactive ion etching. Raman spectroscopy was used to find the regions on the substrate, where the thickness of the graphite flakes corresponded to a monolayer. In the identified regions, the freestanding graphene film was indented using the AFM probes in contact force mode. A Young's modulus of 1 TPa and an intrinsic strength of 130 GPa was reported, which is in good agreement with theoretical prediction for pristine graphene sheet [106], as well as for defect-free single-walled nanotubes [99]. Again, all these studies emphasize the relevance of carefully designed experiments and thorough analysis of experimentally acquired data to validate the theoretical predictions.

4.3 Other One-Dimensional Nanostructures. The experimental techniques discussed above have also been applied to study nanostructures made of other semiconducting and metallic materials such as gallium nitride (GaN), gold, silver, tellurium, and silicon. We will briefly discuss experiments performed on semiconducting gallium nitride and metallic gold and silver nanowires.

Similarly to ZnO, a literature review reveals lack of agreement in the mechanical properties of GaN nanowires. For instance, Nam et al. [107] tested [120] oriented *a*-axis GaN nanowires using the *in situ* dynamic resonance experiments. They observed a size-dependent elastic behavior, opposite in trend to the ZnO nanowires, i.e., the Young's moduli decreased from ~300 GPa (bulk value for GaN) to ~225 GPa as the diameter decreased from 84 nm to 36 nm. On the contrary, Ni et al. [108] performed AFM bending tests on [0001] oriented *c*-axis nanowires (ranging from 60 nm to 110 nm in diameter) by suspending them over a microfabricated trench and measured an average value of 43.9 ± 2.2 GPa for the Young's modulus, independent of the wire diameter. Although the wires investigated in these two studies were differently oriented, the change in magnitude and trends of the elastic moduli are quite drastic. Agrwal et al. [109] performed *in situ* tension tests, using the n-MTS, to study both *a*-axis and *c*-axis nanowires. For *c*-axis NWs, tensile tests revealed a size-independent Young's moduli of ~298 GPa, much higher than the value reported by AFM bending tests, but consistent with the bulk value for GaN [110]. For the *a*-axis nanowires, the Young's modulus was found to be ~213 GPa. Other than semiconducting nanowires, metallic nanowires have also drawn interest because of their low resistivity and possible applications as interconnects in microelectronic devices.

Metallic nanowires, being relatively soft and ductile as compared with semiconducting nanowires, pose greater challenges related to handling and manipulation. In the AFM-based techniques, manipulation of individual nanowire is avoided as the wires are randomly dispersed on a substrate with microfabricated trenches. Using three-point bending technique, as described earlier, Wu et al. [111,112] tested gold nanowires (Fig. 6(*b*)) and reported a size-independent Young's modulus of 70 ± 11 GPa for wires ranging from 40 nm to 250 nm in diameter, which is in agreement with the bulk value of 79 GPa. In contrast, Petrova et al. [113] reported 20–30% decrease in Young's moduli of [100] and [110] oriented nanowires depending on their orientation using time-resolved spectroscopy technique. In this technique, laser induced heating is used to coherently excite acoustic vibrations, and the time period of vibrations is measured to determine the Young's modulus. The softening behavior, observed in spectroscopy experiments, was also confirmed computationally by atomic tension [114,115] and multiscale resonance simulations [116]. This behavior was attributed to surface stress-induced compression. In contrast to the elastic softening observed for gold nanowires, Cuenot et al. [117] reported size-dependent elastic stiffening for silver nanowires employing contact resonance based AFM technique. Young's modulus was reported to increases from a bulk value of 76–140 GPa as the diameter of the nanowires decrease from 70 nm to 30 nm. The fundamental understanding of elastic softening versus stiffening was enhanced by ab initio calculations [118], revealing that there are two competing phenomena, which determine the overall behavior: (i) stiffening gained from the local electronic redistribution on the surfaces; and (ii) softening induced by coordination number reduction due to missing neighbors. Although the simulations predict trends consistent with experimental findings, there is one discrepancy regarding the characteristic size at which the elastic behavior deviates from bulk. For example, for silver nanowires, molecular dynamic simulations reveal that the surface effects are not prominent beyond 20 nm wire diameter [119] as opposed to 70 nm found in experiments [117].

Apart from the elastic behavior, yield strength has also been reported to depend on the nanowire size consistent with findings of earlier studies on thin films and nanopillars. The yield strength of gold nanowires was found to be 5.6 ± 1.4 GPa for 40 nm nanowires as opposed to 3.5 ± 1.1 GPa for larger 200 nm nanowires [111]. For both wire sizes, the measured yield stresses were significantly higher than the bulk value. Similarly, for silver nanowires, higher yield strengths of ~7.3 GPa were reported, as opposed to a value of 55 MPa for bulk silver. Using the n-MTS, "necking" at stresses of ~2.0–2.5 GPa [120] was observed in silver nanowires, as loads were applied in a displacement-controlled fashion. The localized plastic deformation was observed leading to failure at ~6% strain; however, the lower yield stresses (as compared with AFM bending tests) were probably due to the difference in morphologies of the nanowires tested. In general, higher strength values as compared with bulk were hypothesized to be due to dramatic reduction of defect density in the nanowires and the absence or limited number of grains across the nanowire diameter leading to limited emission and absorption of dislocations at the grain boundaries. Computational studies on the plastic behavior of nanowires also predict yield stresses close to the theoretical strength of the material; however, a direct comparison with experiments is lacking due to a few major differences: (i) simulations do not account for defects like missing surface atoms, which are inevitable in the experimentally tested nanowires; (ii) strain rates employed in MD simulations are orders of magnitudes higher than the strain rates achieved experimentally; and (iii) the accuracy of interatomic potentials, used to predict material properties, is not always known. Recently, Zhu et al. [121] analyzed the strain-rate dependence on surface-driven dislocation nucleation for copper nanowires under compression. They reported that defect nucleation stress can be up to 50% lower at strain rates of 10^{-3} s^{-1} as compared with strain rates of 10^{8} s^{-1} (typically found in MD simulations). In addition to the morphological differences

and differences in time scales, the deformation mechanisms revealed by the MD simulations are strongly dependent on the interatomic force fields employed to model the interactions [122,123].

In the earlier phases of development, interatomic potentials for metals were generally developed by arbitrarily choosing certain parameters so as to predict the bulk material properties accurately [124]. In a recent development, Baskes et al. [125] introduced a formalism, which avoids choosing parameters by fitting, but uses first principal calculations of electron densities, embedding energy, pair potential, and angular screening functions. The improved formalism provides a better qualitative agreement with the experimental findings; however, there is no simple force field that can accurately reproduce all relevant material properties. It bears emphasis that the validation of these formulations by comparison to experiments is in its infancy.

5 Concluding Remarks

It can be argued that theory, modeling, and experimentation at the macroscale are quite mature. For instance, various instruments and experimental protocols have been developed to characterized materials and structures under a variety of loading states including fracture and wave propagation. Similarly, continuum theories able to predict material behavior, within a range of loading and deformation conditions, have been advanced and used in engineering design. By contrast, scaling down experiments from macroscale to micro-/nanoscale has not been trivial, as highlighted by the examples discussed in this article. Likewise, continuum theories fail to predict the material behavior at the nanoscale, as surface effects and atomic electronic structures effects become relevant. To include such effects, modeling is done with atomistic details accounting for proper interatomic interactions. The interactions are accurately modeled when first principle calculations are carried out, but such calculations have not been scaled beyond a few hundred atoms because they are computationally too expensive. Semi-empirical or empirical interatomic potential fields have been developed by fitting bulk material properties, with which the model sizes can be scaled up to a few million atoms but at a loss of accuracy and predictive capability. To overcome this limitation, multiscale methods based on quantum mechanics [126,127] should be further developed so that larger simulations can be performed while accounting for atomic scale effects.

In the area of experimentation, microfabrication together with instrumentation possessing nanoscale resolution have played a crucial role in the development of novel techniques for characterization at small scales. For example, thin film studies by wafer curvature measurements, nanoindentation and bulge tests were able to reveal plasticity size effects later investigated in free standing thin films through membrane deflection and in single crystal micropillars through *in situ* electron microscopy experimentation. These later developments made possible one-to-one comparisons with discrete dislocation dynamics predictions of dislocation activation and annihilation leading to an in-depth understanding of the reasons for the observed size effects. Similarly, for one-dimensional nanostructures, a few indirect techniques, such as dynamic resonance and AFM-based nanoindentation, have been able to correctly predict the *qualitative* size-dependent trends. Further insight was gained when the MEMS-based nano-MTS *in situ* electron microscopy setup was employed, which provided unprecedented load and displacement resolution combined with real time atomic imaging allowing correlation of material response to its atomic structure without any assumptions. The strength of this tool was highlighted with two examples—elasticity sized effects in ZnO nanowires and ultimate fracture strength in CNTs—where a direct comparison with computational studies was made possible. The full potential of such a unique technique has not been yet reached in the context of metallic nanostructures, as it should be possible to capture events such as nucleation and propagation of dislocations. The current limitation is that these events leading to plasticity or failure happen over a very short time span (within a few nanoseconds), which is much faster than the scan rate at which imaging can be performed in electron microscopes. To increase the temporal resolution of electron microscopes, dynamic transmission electron microscopy (DTEM) [128,129] was recently demonstrated, with imaging resolution of up to 15 ns. Merging of state-of-the-art techniques, such as nano-MTS and DTEM, seem a natural next step to further enhance the spatial, as well as the temporal resolution of nanoscale experimentation. Along with these advances in experimentation, advancements of computational methods are also necessary to facilitate direct comparisons. This provides a clear direction for future research to further close the gap between experimentation and computer simulations.

References

[1] Park, H. S., Gall, K., and Zimmerman, J. A., 2005, "Shape Memory and Pseudoelasticity in Metal Nanowires," Phys. Rev. Lett., **95**(25), p. 255504.
[2] Diao, J. K., Gall, K., and Dunn, M. L., 2004, "Surface Stress Driven Reorientation of Gold Nanowires," Phys. Rev. B, **70**(7), p. 075413.
[3] Wang, J., Kulkarni, A. J., Ke, F. J., Bai, Y. L., and Zhou, M., 2008, "Novel Mechanical Behavior of ZnO Nanorods," Comput. Methods Appl. Mech. Eng., **197**, pp. 3182–3189.
[4] Gudiksen, M. K., Lauhon, L. J., Wang, J., Smith, D. C., and Lieber, C. M., 2002, "Growth of Nanowire Superlattice Structures for Nanoscale Photonics and Electronics," Nature (London), **415**, pp. 617–619.
[5] Huang, M. H., Mao, S., Feick, H., Yan, H., Wu, Y., Kind, H., Weber, E., Russo, R., and Yang, P., 2001, "Room-Temperature Ultraviolet Nanowire Nanolasers," Science, **292**, pp. 1897–1899.
[6] Wang, Z. L., and Song, J., 2006, "Piezoelectric Nanogenerators Based on Zinc Oxide Nanowire Arrays," Science, **312**, pp. 242–246.
[7] Zhu, Y., and Espinosa, H. D., 2004, "Effect of Temperature on Capacitive RF MEMS Switch Performance—a Coupled-Field Analysis," J. Micromech. Microeng., **14**, pp. 1270–1279.
[8] Mercado, L. L., Lee, T. Y. T., Kuo, S. M., and Amrine, C., 2003, "Thermal Solutions for Discrete and Wafer-Level RF MEMS Switch Packages," IEEE Trans. Adv. Packag., **26**, pp. 318–326.
[9] van Spengen, W. M., Puers, R., Mertens, R., and De Wolf, I., 2003, "A Low Frequency Electrical Test Set-Up for the Reliability Assessment of Capacitive RF MEMS Switches," J. Micromech. Microeng., **13**, pp. 604–612.
[10] Espinosa, H. D., Zhu, Y., Fischer, M., and Hutchinson, J., 2003, "An Experimental/Computational Approach to Identify Moduli and Residual Stress in MEMS Radio-Frequency Switches," Exp. Mech., **43**(3), pp. 309–316.
[11] Doerner, M. F., Gardner, D. S., and Nix, W. D., 1986, "Plastic Properties of Thin Films on Substrates as Measured by Submicron Indentation Hardness and Substrate Curvature Techniques," J. Mater. Res., **1**(6), pp. 845–51.
[12] McInnerney, E. J., and Flinn, P. A., 1982, "Diffusion of Moisture in Thin Films," Proceedings of the 20th IEEE IRPS Symposium, New York.
[13] Pethica, J. B., Hutchings, R., and Oliver, W. C., 1983, *Hardness Measurement at Penetration Depths as Small as 20 nm*, Taylor & Francis, London, pp. 593–606.
[14] Doerner, M. F., and Nix, W. D., 1986, "A Method for Interpreting the Data From Depth-Sensing Indentation Instruments," J. Mater. Res., **1**(4), pp. 601–609.
[15] Venkatraman, R., and Bravman, J. C., 1992, "Separation of Film Thickness and Grain Boundary Strengthening Effects in Al Thin Films on Si," J. Mater. Res., **7**(8), pp. 2040–2048.
[16] Venkatraman, R., Bravman, J. C., Nix, W. D., Avies, P. W. D., Flinn, P. A., and Fraser, D. B., 1990, "Mechanical Properties and Microstructural Characterization of Al-0.5% Cu Thin Films," J. Electron. Mater., **19**(11), pp. 1231–1237.
[17] Oliver, W. C., and Pharr, G. M., 1992, "An Improved Technique for Determining Hardness and Elastic-Modulus Using Load and Displacement Sensing Indentation Experiments," J. Mater. Res., **7**(6), pp. 1564–1583.
[18] Suresh, S., Nieh, T. G., and Choi, B. W., 1999, "Nano-Indentation of Copper Thin Films on Silicon Substrates," Scr. Mater., **41**(9), pp. 951–957.
[19] Gouldstone, A., Koh, H. J., Zeng, K. Y., Giannakopoulos, A. E., and Suresh, S., 2000, "Discrete and Continuous Deformation During Nanoindentation of Thin Films," Acta Mater., **48**(9), pp. 2277–2295.
[20] Saha, R., and Nix, W. D., 2002, "Effects of the Substrate on the Determination of Thin Film Mechanical Properties by Nanoindentation," Acta Mater., **50**(1), pp. 23–38.
[21] Pharr, G. M., and Oliver, W. C., 1992, "Measurement of Thin Film Mechanical Properties Using Nanoindentation," MRS Bull., **17**(7), pp. 28–33.
[22] Vinci, R. P., and Vlassak, J. J., 1996, "Mechanical Behavior of Thin Films," Annu. Rev. Mater. Sci., **26**, pp. 431–462.
[23] Xiang, Y., Chen, X. L., and Vlassak, J. J., 2002, "The Mechanical Properties of Electroplated Cu Thin Films Measured by Means of the Bulge Test Technique," Mater. Res. Soc. Symp. Proc., **695**, pp. L4.9.1–L4.9.6.
[24] Xiang, Y., Tsui, T. Y., and Vlassak, J. J., 2006, "The Mechanical Properties of Freestanding Electroplated Cu Thin Films," J. Mater. Res., **21**(6), pp. 1607–1618.
[25] Xiang, Y., and Vlassak, J. J., 2006, "Bauschinger and Size Effects in Thin-Film Plasticity," Acta Mater., **54**, pp. 5449–5460.

[26] Vlassak, J. J., and Nix, W. D., 1992, "A New Bulge Test Technique for the Determination of Young's Modulus and Poisson Ratio of Thin-Films," Mater. Res. Soc. Symp. Proc., **7**(12), pp. 3242–3249.
[27] Small, M. K., Vlassak, J. J., Powel, S. F., Daniels, B. J., and Nix, W. D., 1993, "Accuracy and Reliability of Bulge Test Experiments," Mater. Res. Soc. Symp. Proc., **308**, pp. 159–164.
[28] Paviot, V. M., Vlassak, J. J., and Nix, W. D., 1995, "Measuring the Mechanical Properties of Thin Metal Films by Means of Bulge Testing of Micromachined Windows," Mater. Res. Soc. Symp. Proc., **356**, pp. 579–584.
[29] Wei, X., Lee, D., Shim, S., Chen, X., and Kysar, J. W., 2007, "Plane-Strain Bulge Test for Nanocrystalline Copper Thin Films," Scr. Mater., **57**, pp. 541–544.
[30] Fleck, N. A., and Hutchinson, J. W., 2001, "A Reformulation of Strain Gradient Plasticity," J. Mech. Phys. Solids, **49**(10), pp. 2245–2271.
[31] Haque, M. A., and Saif, M. T. A., 2002, "Mechanical Behavior of 30–50 nm Thick Aluminum Films Under Uniaxial Tension," Scr. Mater., **47**(12), pp. 863–867.
[32] Minor, A. M., Asif, S. A. S., Shan, Z. W., Stach, E. A., Cryrankowski, E., Wyrobek, T. J., and Warren, O. L., 2006, "A New View of the Onset of Plasticity During the Nanoindentation of Aluminum," Nature Mater., **5**, pp. 697–702.
[33] Espinosa, H. D., Prorok, B. C., and Fischer, M., 2001, "A Novel Experimental Technique For Testing Thin Films and MEMS Materials," Proceedings of the SEM Annual Conference on Experimental and Applied Mechanics, Portland, OR.
[34] Espinosa, H. D., Prorok, B. C., and Fischer, M., 2003, "A Methodology for Determining Mechanical Properties of Freestanding Thin Films and MEMS Materials," J. Mech. Phys. Solids, **51**(1), pp. 47–67.
[35] Espinosa, H. D., Prorok, B. C., Peng, B., Kim, K. H., Moldovan, N., Auciello, O., Carlisle, J. A., Gruen, D. M., and Mancini, D. C., 2003, "Mechanical Properties of Ultrananocrystalline Diamond Thin Films Relevant to MEMS/NEMS Devices," Exp. Mech., **43**, pp. 256–269.
[36] Espinosa, H. D., Peng, B., Prorok, B. C., Moldovan, N., Auciello, O., Carlisle, J. A., Gruen, D. M., and Mancini, D. C., 2003, "Fracture Strength of Ultrananocrystalline Diamond Thin Films—Identification of Weibull Parameters," J. Appl. Phys., **94**(9), pp. 6076–6084.
[37] Espinosa, H. D., Prorok, B. C., and Peng, B., 2004, "Plasticity Size Effects in Free-Standing Submicron Polycrystalline FCC Films Subjected to Pure Tension," J. Mech. Phys. Solids, **52**(3), pp. 667–689.
[38] Yu, D. Y. W., and Spaepen, F., 2004, "The Yield Strength of Thin Copper Films on Kapton," J. Appl. Phys., **95**(6), pp. 2991–2997.
[39] Espinosa, H. D., Berbenni, S., Panico, M., and Schwarz, K., 2005, "An Interpretation of Size-Scale Plasticity in Geometrically Confined Systems," Proc. Natl. Acad. Sci. U.S.A., **102**, pp. 16933–16938.
[40] Haque, M. A., and Saif, M. T. A., 2002, "In-Situ Tensile Testing of Nano-Scale Specimens in SEM and TEM," Exp. Mech., **42**(1), pp. 123–128.
[41] Haque, M. A., and Saif, M. T. A., 2004, "Deformation Mechanisms in Free-Standing Nanoscale Thin Films: A Quantitative *in situ* Transmission Electron Microscope Study," Proc. Natl. Acad. Sci. U.S.A., **101**(17), pp. 6335–6340.
[42] Gianola, D. S., Van Petegem, S., Legros, M., Brandstetter, S., Van Swygenhoven, H., and Hemker, K. J., 2006, "Stress-Assisted Discontinuous Grain Growth and Its Effect on the Deformation Behavior of Nanocrystalline Aluminum Thin Films," Acta Mater., **54**(8), pp. 2253–2263.
[43] Gianola, D. S., Eberl, C., Cheng, X., and Hemker, K. J., 2008, "Stress-Driven Surface Topography Evolution in Nanocrystalline Al Thin Films," Adv. Mater., **20**, pp. 303–308.
[44] Gianola, D. S., and Sharpe, W. N., 2004, "Techniques for Testing Thin Films in Tension," Exp. Tech., **28**(5), pp. 23–27.
[45] Rajagopalan, J., Han, J. H., and Saif, M. T. A., 2007, "Plastic Deformation Recovery in Freestanding Nanocrystalline Aluminum and Gold Thin Films," Science, **315**, pp. 1831–1834.
[46] Robertson, I. M., 1986, "Microtwin Formation in Deformed Nickel," Philos. Mag. A, **54**(6), pp. 821–835.
[47] Robertson, I. M., Lee, T. C., Rozenak, P., Bond, G. M., and Birnbaum, H. K., 1989, "Dynamic Observations of the Transfer of Slip Across a Grain-Boundary," Ultramicroscopy, **30**(1–2), pp. 70–75.
[48] Robertson, I. M., Vetrano, J. S., Kirk, M. A., and Jenkins, M. L., 1991, "On the Formation of Vacancy Type Dislocation Loops from Displacement Cascades in Nickel," Philos. Mag. A, **63**(2), pp. 299–318.
[49] Matsukawa, Y., and Zinkle, S. J., 2004, "Dynamic Observation of the Collapse Process of a Stacking Fault Tetrahedron by Moving Dislocations," J. Nucl. Mater., **329–333**, pp. 919–923.
[50] Matsukawa, Y., Osetsky, Y. N., Stoller, R. E., and Zinkle, S. J., 2005, "The Collapse of Stacking-Fault Tetrahedra by Interaction With Gliding Dislocations," Mater. Sci. Eng., A, **400–401**, pp. 366–369.
[51] Osetsky, Y. N., Matsukawa, Y., Stoller, R. E., and Zinkle, S. J., 2006, "On the Features of Dislocation-Obstacle Interaction in Thin Films: Large-Scale Atomistic Simulation," Philos. Mag. Lett., **86**(8), pp. 511–519.
[52] Stach, E. A., Freeman, T., Minor, A. M., Owen, D. K., Cumings, J., Wall, M. A., Chraska, T., Hull, R., Morris, J. J. W., Zettl, A., and Dahmen, U., 2001, "Development of a Nanoindenter for In-Situ Transmission Electron Microscopy," Microsc. Microanal., **7**(6), pp. 507–517.
[53] Minor, A. M., Morris, J. J. W., and Stach, E. A., 2001, "Quantitative *in situ* Nanoindentation in an Electron Microscope," Appl. Phys. Lett., **79**(11), pp. 1625–1627.
[54] Minor, A. M., Lilleodden, E. T., Stach, E. A., and Morris, J. J. W., 2004, "Direct Observations of Incipient Plasticity During Nanoindentation of Al," J. Mater. Res., **19**(1), pp. 176–182.
[55] Uchic, M. D., and Dimiduk, D. M., 2005, "A Methodology to Investigate Size Scale Effects in Crystalline Plasticity Using Uniaxial Compression Testing," Mater. Sci. Eng., A, **400–401**, pp. 268–278.
[56] Uchic, M. D., Dimiduk, D. M., Florando, J. N., and Nix, W. D., 2004, "Sample Dimensions Influence Strength and Crystal Plasticity," Science, **305**, pp. 986–989.
[57] Greer, J. R., Oliver, W. C., and Nix, W. D., 2005, "Size Dependence of Mechanical Properties of Gold at the Micron Scale in the Absence of Strain Gradients," Acta Mater., **53**(6), pp. 1821–1830.
[58] Shan, Z. W., Mishra, R. K., Asif, S. A. S., Warren, O. L., and Minor, A. M., 2007, "Mechanical Annealing and Source-Limited Deformation in Submicrometer-Diameter Ni Crystals," Nature Mater., **7**, pp. 115–119.
[59] Tang, H., Schwarz, K. W., and Espinosa, H. D., 2007, "Dislocation Escape-Related Size Effects in Single-Crystal Micropillars Under Uniaxial Compression," Acta Mater., **55**, pp. 1607–1616.
[60] Tang, H., Schwarz, K. W., and Espinosa, H. D., 2008, "Dislocation-Source Shutdown and the Plastic Behavior of Single-Crystal Micropillars," Phys. Rev. Lett., **100**(18), p. 185503.
[61] Madec, R., Devincre, B., Kubin, L., Hoc, T., and Rodney, D., 2003, "The Role of Collinear Interaction in Dislocation-Induced Hardening," Science, **301**, pp. 1879–1882.
[62] Greer, J. R., and Nix, W. D., 2006, "Nonoscale Gold Pillars Strengthened Through Dislocation Starvation," Phys. Rev. B, **73**, p. 245410.
[63] Cui, Y., Wei, Q., Park, H., and Lieber, C. M., 2001, "Nanowire Nanosensors for Highly Sensitive and Selective Detection of Biological and Chemical Species," Science, **293**(5533), pp. 1289–1292.
[64] Bai, X. D., Gao, P. X., Wang, Z. L., and Wang, E. G., 2003, "Dual-Mode Mechanical Resonance of Individual ZnO Nanobelts," Appl. Phys. Lett., **82**(26), pp. 4806–4808.
[65] Simmons, G., and Wang, H., 1971, *Single Crystal Elastic Constants and Calculated Aggregate Properties*, MIT Press, Cambridge, MA.
[66] Chen, C. Q., Shi, Y., Zhang, Y. S., Zhu, J., and Yan, Y. J., 2006, "Size Dependence of Young's Modulus in ZnO Nanowires," Phys. Rev. Lett., **96**, p. 075505.
[67] Ni, H., and Li, X., 2006, "Young's Modulus of ZnO Nanobelts Measured using Atomic Force Microscopy and Nanoindentation Techniques," Nanotechnology, **17**, pp. 3591–3597.
[68] Song, J., Wang, X., Riedo, E., and Wang, Z. L., 2005, "Elastic Property of Vertically Aligned Nanowires," Nano Lett., **5**(10), pp. 1954–1958.
[69] Hoffmann, S., Ostlund, F., Michler, J., Fan, H. J., Zacharias, M., Christiansen, S. H., and Ballif, C., 2007, "Fracture Strength and Young's Modulus of ZnO Nanowires," Nanotechnology, **18**, pp. 205503.
[70] Zhou, P., Wu, C., and Li, X., 2008, "Three-Point Bending Young's Modulus of Nanowires," Meas. Sci. Technol., **19**(11), p. 115703.
[71] Poncharal, P., Wang, Z. L., Ugarte, D., and de Heer, W. A., 1999, "Electrostatic Deflections and Electromechanical Resonances of Carbon Nanotubes," Science, **283**(5407), pp. 1513–1516.
[72] Salvetat, J. P., Briggs, G. A. D., Bonard, J. M., Bacsa, R. R., Kulik, A. J., Stockli, T., Burnham, N. A., and Forro, L., 1999, "Elastic and Shear Moduli of Single-Walled Carbon Nanotube Ropes," Phys. Rev. Lett., **82**(5), pp. 944–947.
[73] Yu, M. F., Lourie, O., Dyer, M. J., Moloni, K., Kelly, T. F., and Ruoff, R. S., 2000, "Strength and Breaking Mechanism of Multiwalled Carbon Nanotubes Under Tensile Load," Science, **287**(5453), pp. 637–640.
[74] Stan, G., Ciobanu, C. V., Parthangal, P. M., and Cook, R. F., 2007, "Diameter-Dependent Radial and Tangential Elastic Moduli of ZnO Nanowires," Nano Lett., **7**(12), pp. 3691–3697.
[75] Stan, G., Krylyuk, S., Davydov, A. V., Vaudin, M., Bendersky, L. A., and Cook, R. F., 2008, "Surface Effects on the Elastic Modulus of Te Nanowires," Appl. Phys. Lett., **92**, p. 241908.
[76] Desai, A. V., and Haque, M. A., 2006, "Mechanical Properties of ZnO Nanowires," Sens. Actuators, A, **134**(1), pp. 169–176.
[77] Samuel, B. A., Desai, A. V., and Haque, M. A., 2006, "Design and Modeling of a MEMS Pico-Newton Loading/Sensing Device," Sens. Actuators, A, **127**, pp. 155–162.
[78] Agrawal, R., Peng, B., Gdoutos, E. E., and Espinosa, H. D., 2008, "Elasticity Size Effects in ZnO Nanowires—a Combined Experimental-Computational Approach," Nano Lett., **8**(11), pp. 3668–3674.
[79] Zhu, Y., Moldovan, N., and Espinosa, H. D., 2005, "A Microelectromechanical Load Sensor for *in situ* Electron and X-Ray Microscopy Tensile Testing of Nanostructures," Appl. Phys. Lett., **86**(1), pp. 013506.
[80] Zhu, Y., Corigliano, A., and Espinosa, H. D., 2006, "A Thermal Actuator for Nanoscale In-Situ Microscopy Testing: Design and Characterization," J. Micromech. Microeng., **16**, pp. 242–253.
[81] Zhu, Y., and Espinosa, H. D., 2005, "An Electromechanical Material Testing System for *in situ* Electron Microscopy and Applications," Proc. Natl. Acad. Sci. U.S.A., **102**(41), pp. 14503–14508.
[82] Espinosa, H. D., Zhu, Y., and Moldovan, N., 2007, "Design and Operation of a MEMS-Based Material Testing System for Nanomechanical Characterization," J. Microelectromech. Syst., **16**(5), pp. 1219–1231.
[83] Iijima, S., 1991, "Helical Microtubules of Graphitic Carbon," Nature (London), **354**, pp. 56–58.
[84] Koziol, K., Vilatela, J., Moisala, A., Motta, M., Cunniff, P., Sennett, M., and Windle, A., 2007, "High-Performance Carbon Nanotube Fiber," Science, **318**, pp. 1892–1896.
[85] Tans, S. J., Verschueren, A. R. M., and Dekker, C., 1998, "Room-Temperature

Transistor Based on a Single Carbon Nanotube," Nature (London), **393**, pp. 49–52.
[86] Hu, J., Ouyang, M., Yang, P., and Lieber, C. M., 1999, "Controlled Growth and Electrical Properties of Heterojunctions of Carbon Nanotubes and Silicon Nanowires," Nature (London), **399**, pp. 48–51.
[87] Odom, T. W., Huang, J.-L., and Lieber, C. M., 2002, "Single-Walled Carbon Nanotubes: From Fundamental Studies to New Device Concepts," Ann. N. Y. Acad. Sci., **960**, pp. 203–215.
[88] Ouyang, M., Huang, J.-L., and Lieber, C. M., 2002, "Fundamental Electronic Properties and Applications of Single-Walled Carbon Nanotubes," Acc. Chem. Res., **35**, pp. 1018–1025.
[89] Ogata, S., and Shibutani, Y., 2003, "Ideal Tensile Strength and Band Gap of Single-Walled Carbon Nanotubes," Phys. Rev. B, **68**, p. 165409.
[90] Ozaki, T., Iwasa, Y., and Mitani, T., 2000, "Stiffness of Single-Walled Carbon Nanotubes Under Large Strain," Phys. Rev. Lett., **84**, pp. 1712–1715.
[91] Dumitrica, T., Belytschko, T., and Yakobson, B. I., 2003, "Bond-Breaking Bifurcation States in Carbon Nanotube Fracture," J. Chem. Phys., **118**, pp. 9485–9488.
[92] Troya, D., Mielke, S. L., and Schatz, G. C., 2003, "Carbon Nanotube Fracture—Differences Between Quantum Mechanical Mechanisms and those of Empirical Potentials," Chem. Phys. Lett., **382**, pp. 133–141.
[93] Peng, B., Locascio, M., Zapol, P., Li, S., Mielke, S., Schatz, G., and Espinosa, H. D., 2008, "Measurements of Near-Ultimate Strength for Multiwalled Carbon Nanotubes and Irradiation-Induced Crosslinking Improvements," Nat. Nanotechnol., **3**(10), pp. 626–631.
[94] Stach, E. A., 2008, "Nanotubes Reveal Their True Strength," Nat. Nanotechnol., **3**, pp. 586–587.
[95] Treacy, M. M. J., Ebbesen, T. W., and Gibson, J. M., 1996, "Exceptionally High Young's Modulus Observed for Individual Carbon Nanotubes," Nature (London), **381**(6584), pp. 678–680.
[96] Wong, E., Sheehan, P., and Lieber, C., 1997, "Nanobeam Mechanics: Elasticity, Strength, and Toughness of Nanorods and Nanotubes," Science, **277**, pp. 1971–1975.
[97] Walters, D. A., Ericson, L. M., Casavant, M. J., Liu, J., Colbert, D. T., Smith, K. A., and Smalley, R. E., 1999, "Elastic Strain of Freely Suspended Single-Wall Carbon Nanotube Ropes," Appl. Phys. Lett., **74**(25), pp. 3803–3805.
[98] Salvetat, J. P., Kulik, A. J., Bonard, J. M., Briggs, G. A. D., Stockli, T., Metenier, K., Bonnamy, S., Beguin, F., Burnham, N. A., and Forro, L., 1999, "Elastic Modulus of Ordered and Disordered Multiwalled Carbon Nanotubes," Adv. Mater., **11**(2), pp. 161–165.
[99] Mielke, S. L., Troya, D., Sulin, Z., Li, J.-L., Shaoping, X., Roberto, C. A. R., Ruoff, R. S., Schatz, G. C., and Belytschko, T., 2004, "The Role of Vacancy Defects and Holes in the Fracture of Carbon Nanotubes," Chem. Phys. Lett., **390**(4–6), pp. 413–420.
[100] Mielke, S. L., Zhang, S., Khare, R., Ruoff, R. S., Belytschko, T., and Schatz, G. C., 2007, "The Effects of Extensive Pitting on the Mechanical Properties of Carbon Nanotubes," Chem. Phys. Lett., **446**, pp. 128–132.
[101] Ding, W., Calabri, L., Kohlhaas, K. M., Chen, X., Dikin, D. A., and Ruoff, R. S., 2007, "Modulus, Fracture Strength, and Brittle Vs. Plastic Response of the Outer Shell of Arc Grown Multi-Walled Carbon Nanotubes," Exp. Mech., **47**, pp. 25–26.
[102] Barber, A. H., Kaplan-Ashiri, I., Cohen, S. R., Tenne, R., and Wagner, H. D., 2005, "Stochastic Strength of Nanotubes: An Appraisal of Available Data," Compos. Sci. Technol., **65**, pp. 2380–2384.
[103] Barber, A. H., Andrews, R., Schadler, L. S., and Wagner, H. D., 2005, "On the Tensile Strength Distribution of Multiwalled Carbon Nanotubes," Appl. Phys. Lett., **87**(203106), pp. 1–3.
[104] Smith, B. W., and Luzzi, D. E., 2001, "Electron Irradiation Effects in Single Wall Carbon Nanotubes," J. Appl. Phys., **90**, pp. 3509–3515.
[105] Lee, C., Wei, X., Kysar, J. W., and Hone, J., 2008, "Measurement of the Elastic Properties and Intrinsic Strength of Monolayer Graphene," Science, **321**, pp. 385–388.
[106] Khare, R., Mielke, S. L., Paci, J. T., Zhang, S., Ballarini, R., Schatz, G. C., and Belytschko, T., 2007, "Coupled Quantum Mechanical/Molecular Mechanical Modeling of the Fracture of Defective Carbon Nanotubes and Graphene Sheets," Phys. Rev. B, **75**, p. 075412.
[107] Nam, C.-Y., Jaroenapibal, P., Tham, D., Luzzi, D. E., Evoy, S., and Fischer, J. E., 2006, "Diameter-Dependent Electromechanical Properties of GaN Nanowires," Nano Lett., **6**(2), pp. 153–158.
[108] Ni, H., Li, X., Cheng, G., and Klie, R., 2006, "Elastic Modulus of Single-Crystal GaN Nanowires," J. Mater. Res., **21**(11), pp. 2882–2887.
[109] Agrawal, R., B. Peng, and H.D. Espinosa, 2009, "The Effect of Growth Orientation and P-Type Doping on the Elastic Modulus and Fracture of Single-Crystal GaN Nanowires," to be published.
[110] Schwarz, R. B., Khachaturan, K., and Weber, E. R., 1997, "Elastic Moduli of Gallium Nitride," Appl. Phys. Lett., **70**(9), pp. 1122–1124.
[111] Wu, B., Heidelberg, A., and Boland, J. J., 2005, "Mechanical Properties of Ultrahigh-Strength Gold Nanowires," Nature Mater., **4**(7), pp. 525–529.
[112] Wu, B., Heidelberg, A., Boland, J. J., Sader, J. E., Sun, X. M., and Li, Y. D., 2006, "Microstructure-Hardened Silver Nanowires," Nano Lett., **6**(3), pp. 468–472.
[113] Petrova, H., Jorge, P.-J., Zhenyuan, Z., Zhang, J., Kosel, T., and Hartland, G. V., 2006, "Crystal Structure Dependence of the Elastic Constants of Gold Nanorods," J. Mater. Chem., **16**, pp. 3957–3963.
[114] Liang, H., Upmanyu, M., and Huang, H., 2005, "Size-Dependent Elasticity of Nanowires: Nonlinear Effects," Phys. Rev. B, **71**(24), pp. 241403.
[115] Diao, J., Gall, K., and Dunn, M. L., 2004, "Atomistic Simulation of the Structure and Elastic Properties of Gold Nanowires," J. Mech. Phys. Solids, **52**(9), pp. 1935–1962.
[116] Park, H. S., and Klein, P. A., 2008, "Surface Stress Effects on the Resonant Properties of Metal Nanowires: The Importance of Finite Deformation Kinematics and the Impact of the Residual Surface Stress," J. Mech. Phys. Solids, **56**(11), pp. 3144–3166.
[117] Cuenot, S., Fretigny, C., Demoustier-Champagne, S., and Nysten, B., 2004, "Surface Tension Effect on the Mechanical Properties of Nanomaterials Measured by Atomic Force Microscopy," Phys. Rev. B, **69**, p. 165410.
[118] Zhou, L. G., and Huang, H., 2004, "Are Surface Elastically Softer or Stiffer," Appl. Phys. Lett., **84**(11), pp. 1940–1942.
[119] McDowell, M. T., Leach, A. M., and Gall, K., 2008, "Bending and Tensile Deformation of Metallic Nanowires," Modell. Simul. Mater. Sci. Eng., **16**(045003), pp. 1–13.
[120] Peng, B., Sun, Y. G., Zhu, Y., Wang, H.-H., and Espinosa, H. D., 2008, "Nanoscale Testing of One-Dimensional Nanostructures," *Micro and Nano Mechanical Testing of Materials and Devices*, F. Yang and C. J. M. Li, eds., Springer, New York, pp. 287–311.
[121] Zhu, T., Li, J., Samanta, A., Leach, A., and Gall, K., 2008, "Temperature and Strain-Rate Dependence of Surface Dislocation Nucleation," Phys. Rev. Lett., **100**, p. 025502.
[122] Van Swygenhoven, H., Derlet, P. M., and Froseth, A. G., 2004, "Stacking Fault Energies and Slip in Nanocrystalline Metals," Nature Mater., **3**, pp. 399–403.
[123] Van Swygenhoven, H., 2006, "Dislocation Propagation Versus Dislocation Nucleation," Nature Mater., **5**, p. 841.
[124] Baskes, M. I., 1992, "Modified Embedded-Atom Potentials for Cubic Materials and Impurities," Phys. Rev. B, **46**(5), pp. 2727–2742.
[125] Baskes, M. I., Srinivasan, S. G., Valone, S. M., and Hoagland, R. G., 2007, "Multistate Modified Embedded Atoms Method," Phys. Rev. B, **75**, p. 094113.
[126] Gavini, V., Bhattacharya, K., and Ortiz, M., 2007, "Quasi-Continuum Orbital-Free Density-Functional Theory: A Route to Multi-Million Atom Non-Periodic DFT Calculation," J. Mech. Phys. Solids, **55**, pp. 697–718.
[127] Fago, M., Hayes, R. L., Carter, E. A., and Ortiz, M., 2004, "Density-Functional-Theory-Based Local Quasicontinuum Method: Prediction of Dislocation Nucleation," Phys. Rev. B, **70**, p. 100102.
[128] Armstrong, M. R., Boyden, K., Browning, N. D., Campbell, G. H., Colvin, J. D., DeHope, W. J., Frank, A. M., Gibson, D. J., Hartemann, F., Kim, J. S., King, W. E., LaGrange, T. B., Pyke, B. J., Reed, B. W., Shuttlesworth, R. M., Stuart, B. C., and Torralva, B. R., 2007, "Practical Considerations for High Spatial and Temporal Resolution Dynamic Transmission Electron Microscopy," Ultramicroscopy, **107**, pp. 356–367.
[129] Kim, J. S., LaGrange, T., Reed, B. W., Taheri, M. L., Armstrong, M. R., King, W. E., Browning, N. D., and Campbell, G. H., 2008, "Imaging of Transient Structures Using Nanosecond *in situ* TEM," Science, **321**(5895), pp. 1472–1475.